Supplemental Information for

A Rare Isocyanide Derived from an Unprecedented Neutral Yttrium(II) Bis(amide) Complex

Rashmi Jena, Florian Benner, Francis Delano IV, Daniel Holmes, John McCracken,* Selvan Demir,* and

Aaron L. Odom*

Michigan State University, Department of Chemistry, 578 S. Shaw Lane, East Lansing, Michigan 48824

*Correspondence to: odoma@msu.edu (A.L.O.), sdemir@chemistry.msu.edu (S.D.), mccracke@msu.edu
(J. M.)

Table of Contents

General Considerations

   All manipulations are done under purified nitrogen atmosphere in either a glove box or using Schlenk techniques. Hexamethyldisiloxane (HDMSO) and *n*-hexane were dried with CaH_2, distilled under nitrogen to remove oxygen and stored over 4 Å molecular sieves. Tetrahydrofuran was dried with Na/benzophenone, distilled under nitrogen to remove oxygen, and stored over 4 Å molecular sieves. 2,6-dichloroiodobenzene was purchased from Oakwood and, after freeze-pump-thawing three times to remove dissolved gases, was transferred into the glovebox. *tert*-Butyl isocyanide and trimethylacetonitrile were purchased from Sigma-Aldrich and, after freeze-pump-thawing three times to remove dissolved gases, were passed through activated alumina before use. YCl_3 and trimethylsilylmethyllithium solution in pentane (0.1 M) were purchased from Sigma-Aldrich and used as received. Trimethylsilylmethylpotassium and tosyl azide were synthesized according to the literature procedure.[1,2] H_2NAr* was also synthesized according to the literature procedure,[3,4] and ^{1}H NMR spectra matched with reported data.[3]

   NMR solvents C_6D_6 and C_7D_8 were purchased from Cambridge Isotope Laboratories, Inc. C_6D_6 and C_7D_8 are distilled over CaH_2 and passed through activated alumina to ensure drying. Both NMR solvents were stored under an inert atmosphere. The NMR spectra were taken on Varian or Bruker instruments located in the Max T. Rogers Instrumentation facility at Michigan State University. ^{1}H and ^{13}C NMR spectra were recorded on a Bruker Avance Neo 600 MHz spectrometer. [89]Y NMR spectra were collected on Bruker Avance III HD 500 MHz spectrometer operating at 24.5 MHz for [89]Y. NMR chemical shifts are reported in ppm and reference to the solvent peaks for ^{1}H NMR (C_6D_6, δ 7.16 ppm; C_7D_8, δ 2.08, 6.97, 7.01, 7.09 ppm), ^{13}C NMR (C_6D_6, δ 128.06 ppm; C_7D_8, δ 20.43, 125.13, 127.96 ppm). [89]Y NMR data was referenced using vendor supplied method of indirect referencing (Bruker TopSpin 3.6.2) relative to the lock solvent and aqueous $Y(NO_3)_3$. This method is based on IUPAC recommendations for indirect referencing.[5] Referencing derived from the 1D NMR data were used to calibrate the 2D ^{1}H-[89]Y HMBC experiments.

Single crystal data was collected on XtaLAB Synergy, Dualflex, Hypix diffractometer using CuK$_\alpha$ radiation. Data collection was done at 100 K under a continuous flow of liquid nitrogen. In Olex2 program, crystal structures were solved with ShelXT solution using intrinsic phasing and refined with the SheXL refinement package using least squares minimization.[6,7] All hydrogens are refined anisotropically. All crystals were stable at room temperature for mounting. Experimental details for IR spectroscopy, EPR Spectroscopy and Cyclic Voltammetry are mentioned in their respective sections.

Synthesis of Complexes

Synthesis of KNHAr*: A 20 mL scintillation vial charged with a stir bar was loaded with 2,6-Tripp$_2$C$_6$H$_3$NH$_2$ (500.3 mg, 1.0 mmol, 1.0 equiv.) and *n*-hexane (15 mL). This solution was kept in the freezer for 15 min. This solution was kept on a stir plate and then trimethylsilylmethyl potassium (133.3 mg, 1.0 mmol, 1.05 equiv.) was added slowly. The solution was left to stir for 12 h at room temperature. The reaction mixture was filtered (using a fritted funnel), washed with cold *n*-hexane, and dried under reduced pressure. The pure product was obtained as a colorless solid (433.0 mg, 0.80 mmol, 80% yield). ^{1}H NMR (500 MHz, C$_6$D$_6$) δ 7.12 (s, 4H), 7.04 (d, *J* = 7.1 Hz, 2H), 6.56 (t, *J* = 7.1 Hz, 1H), 3.52-3.38 (m, 4H), 2.88-2.73 (m, 2H), 2.62 (s, 1H), 1.27 (t, *J* = 7.3 Hz, 24H), 1.23 (d, *J* = 6.8 Hz, 12H). The compound should not be recrystallized as this leads to contamination with H$_2$NAr* and formation of an insoluble solid, which is likely K$_2$NAr*.

Synthesis of Y(NHAr)$_2$Cl (1)*: A 20 mL scintillation vial charged with a stir bar was loaded with YCl$_3$ (27.30 mg, 0.14 mmol, 1.0 equiv.) and Et$_2$O (5 mL). A separate 20 mL scintillation vial was loaded with KNHAr* (150.0 mg, 0.28 mmol, 2.0 equiv.) and Et$_2$O (5 mL). Both solutions were cooled in a dry ice/acetone cold well for 20 minutes and then the YCl$_3$ solution was suspended above a magnetic stir bar. When the solution had thawed enough to stir, a cold solution of KNHAr* was added dropwise. The solution was left to stir for 12 h at room temperature. The reaction color changed from pale yellow to dark yellow over the period of 12 h. The volatiles were removed in vacuo. The resulting yellow solid was extracted with *n*-hexane and

the solvent was removed in vacuo. A concentrated solution in *n*-hexane resulted in the formation of yellow-colored X-ray quality single crystals overnight at −35 °C in the freezer (100.0 mg, 0.090 mmol, 64% yield). Anal. Calcd for $C_{72}H_{100}N_2YCl$: C, 77.35; H, 9.01; N, 2.50. Found: C, 77.07; H, 9.46; N, 2.46. ^{1}H NMR (600 MHz, C_7D_8) δ 7.25 (s, 8H), 6.92 (d, *J* = 7.4 Hz, 4H), 6.67 (t, *J* = 7.4 Hz, 2H), 4.51 (s, 2H), 2.97 (hept, *J* = 6.8 Hz, 8H), 2.82 (p, *J* = 6.9 Hz, 4H), 1.32 (d, *J* = 6.9 Hz, 24H), 1.28 (d, *J* = 7.0 Hz, 24H), 1.10 (d, *J* = 6.8 Hz, 24H). ^{13}C NMR (151 MHz, C_7D_8) δ 156.54, 156.51, 149.47, 148.80, 137.45, 130.67, 129.00, 128.84, 128.68, 128.09, 127.92, 127.77, 126.14, 125.26, 125.10, 124.93, 123.49, 120.45, 114.65, 34.48, 31.12, 25.51, 24.56, 24.29, 23.91, 20.78, 20.65, 20.40, 20.15, 20.02. [89]Y NMR (25 MHz, C_7D_8) δ 427.73. Decomposition temperature: 190 °C.

Synthesis of Y(NHAr*)$_2$ (2): A 20 mL scintillation vial charged with crystals of **1** (60.0 mg, 0.05 mmol, 1.0 equiv.), 5 mL THF, and a magnetic stir bar. The vial was placed in a liquid nitrogen-cooled cold well until the solution froze. Once frozen, the vial was removed from the cold well and suspended above a magnetic stir plate. When the solution had thawed enough to stir, a suspension of KC_8 (14.5 mg, 0.10 mmol, 2.0 equiv.) in THF (2 mL) was added. The solution turned color from yellow to black rapidly. The solution was stirred for 1 h at room temperature. The volatiles were then removed under reduced pressure, and the remaining residue dissolved in 3 mL of diethyl ether. The ether solution was stirred for ~5 min and filtered using Celite. The filtrate was then dried in vacuo to remove volatiles. The remaining black residue was dissolved in *n*-hexane and filtered using Celite twice. X-ray quality single crystals were produced by chilling a concentrated *n*-hexane solution of **1** in a −35 °C freezer overnight (30.7 mg, 0.02 mmol, 52% yield). Anal. Calcd for $C_{72}H_{100}N_2Y$: C, 77.35; H, 9.01; N, 2.50. $C_{72}H_{100}N_2Y \cdot C_4H_8O$: C, 79.05; H, 9.43; N, 2.43. Found: C, 78.90; H, 9.77; N, 2.33. ^{1}H NMR and ^{13}C NMR spectra did not show any distinctive peaks for the paramagnetic complex. EPR (in manuscript) and UV-vis/NIR spectra (below) were recorded.

Synthesis of Y(NHAr*)₂NC (3): A 20 mL scintillation vial was charged with crystals of **2** (49.5 mg, 0.04 mmol, 1.0 equiv.), 3 mL n-hexane, and a magnetic stir bar. A separate 20 mL scintillation vial was loaded with *tert*-butylisonitrile (3.60 mg, 0.04 mmol, 1.0 equiv.) and 2 mL *n*-hexane. Both solutions were cooled in a dry ice/acetone cold well for 20 minutes and then CN^{t}Bu solution was added dropwise into the solution of **2**. The reaction color changed from black to pale yellow rapidly. The reaction mixture was allowed to stir for 30 minutes. The solvent was removed in vacuo and the resulting yellow solid was extracted with *n*-hexane and solvent was removed. A concentrated solution in *n*-hexane resulted in the formation of yellow-colored X-ray quality single crystals overnight at −35 °C in the freezer (31.6 mg, 0.03 mmol, 67% yield). Anal. Calcd for $C_{73}H_{100}N_3Y$: C, 79.02; H, 9.09; N, 3.79. Found: C, 78.50; H, 9.28; N, 3.62. ^{1}H NMR (600 MHz, C_7D_8) δ 7.29 (s, 2H), 6.91 (d, *J* = 7.4 Hz, 2H), 6.67 (t, *J* = 7.4 Hz, 1H), 4.65 (d, *J* = 1.6 Hz, 1H), 3.05-2.86 (m, 3H), 1.36 (d, *J* = 7.0 Hz, 9H), 1.26 (d, *J* = 5.0 Hz, 1H), 1.09 (d, *J* = 6.8 Hz, 8H). ^{13}C NMR (151 MHz, C_7D_8) δ 181.18 (d, $^2J_{Y-C}$ = 9.8 Hz), 156.55 (d, $^2J_{Y-Car}$ = 3.3 Hz), 149.31, 149.09, 137.46, 130.40, 126.15, 115.03, 34.57, 31.33, 25.07, 24.25, 24.09. [89]Y NMR (25 MHz, C_6D_6) δ 350.28. Decomposition temperature: 184 °C. An NMR scale reaction was set up using trimethylacetonitrile as starting material instead of *tert*-butylisonitrile, and the same product was observed by ^{1}H NMR labeled as **3a**.

NMR Spectra of Complexes 1 and 3
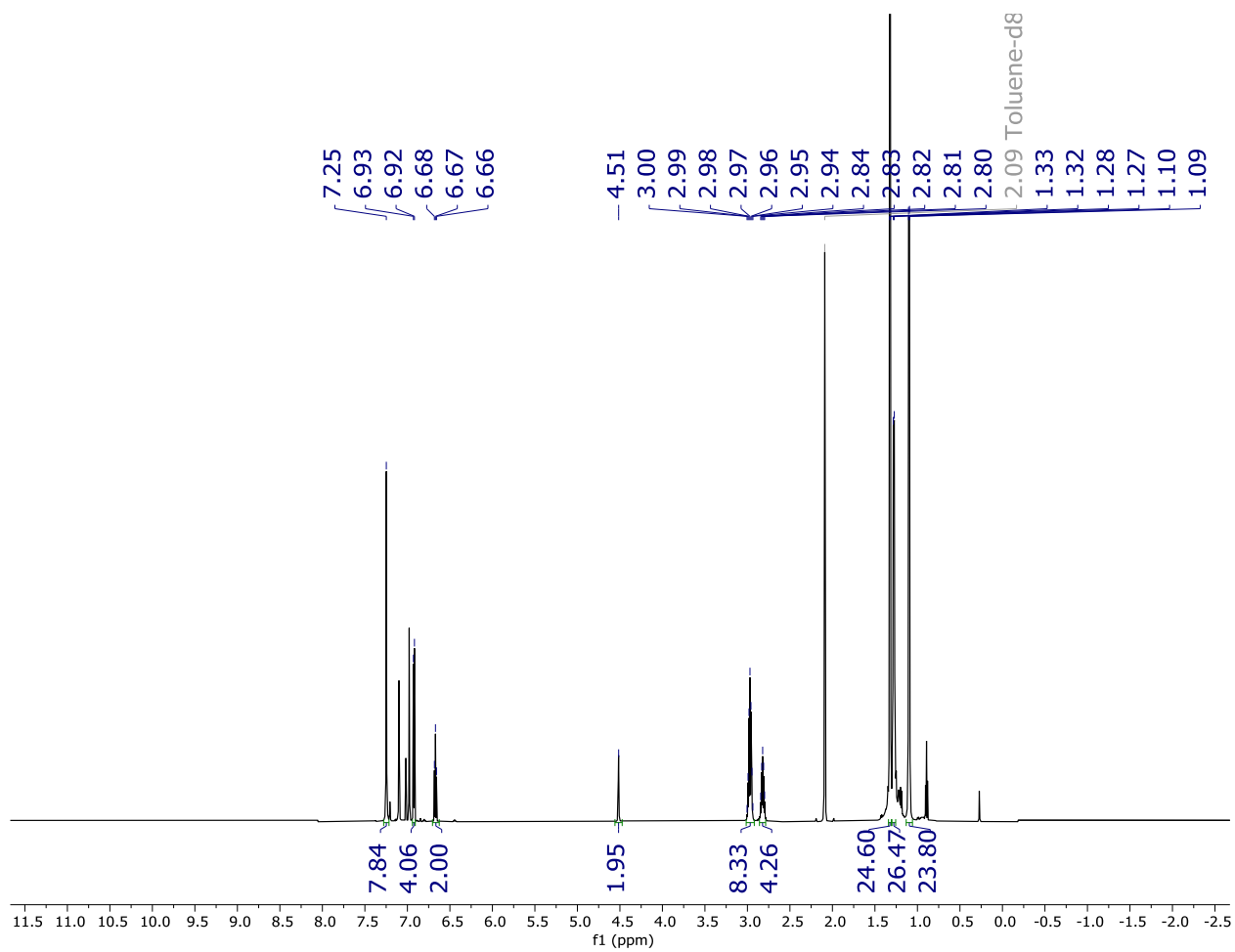
Figure S1. *^1H NMR spectrum of Y(NHAr*)$_2$Cl (**1**) in C$_7$D$_8$.*

156.54
156.51
149.47
148.80
130.67
126.14
123.49
120.45
114.65
34.48
31.12
25.51
24.56
24.29
23.91
20.40 Toluene-d8

f1 (ppm)
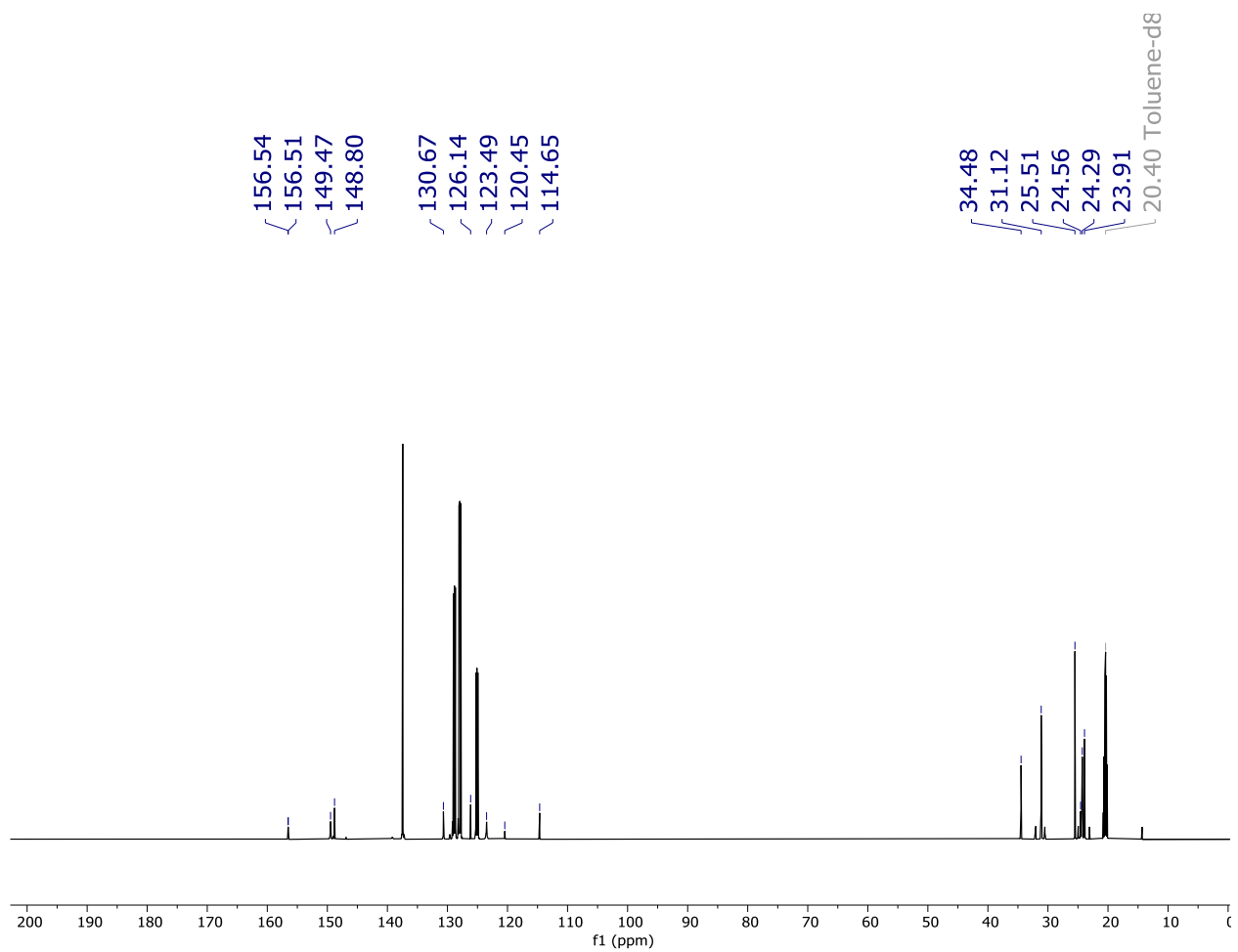
Figure S2. ^{13}C NMR spectrum of Y(NHAr*)$_2$Cl (**1**) in C$_7$D$_8$.
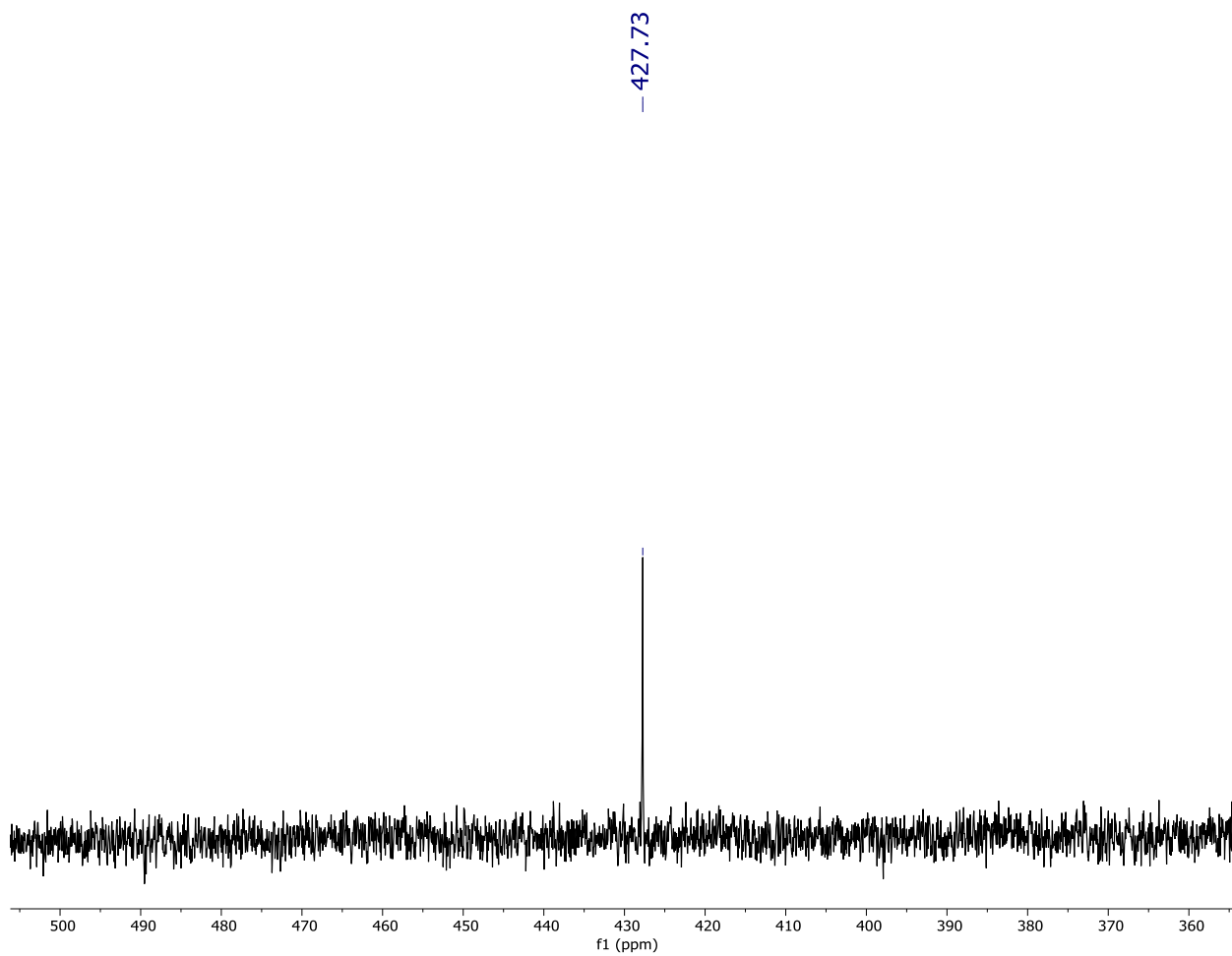
Figure S3. ^{89}Y NMR spectrum of Y(NHAr*)$_2$Cl (**1**) (18 mM) in C$_7$D$_8$.
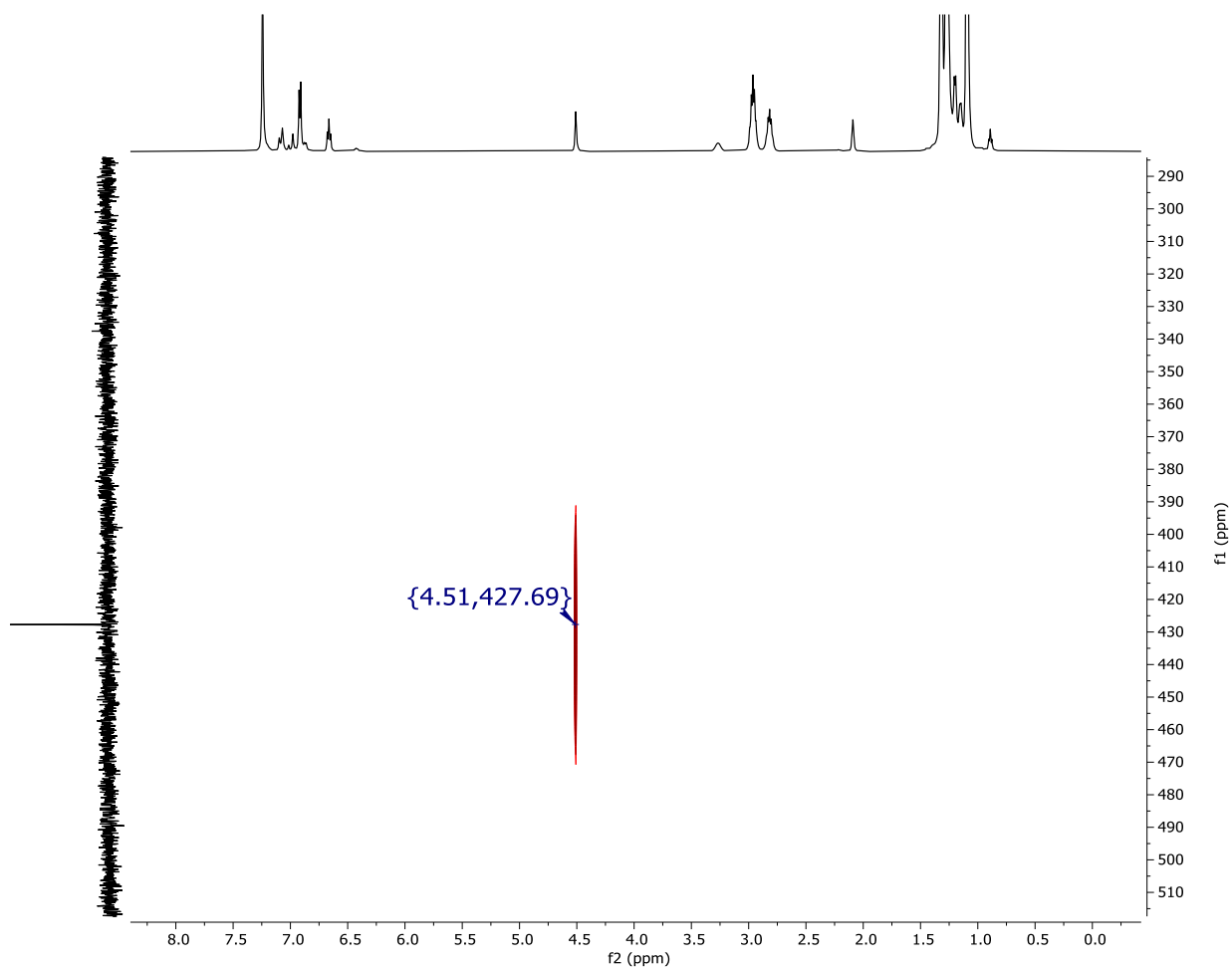
Figure S4. *HMBC for ^1H–^{89}Y spectrum of Y(NHAr*)$_2$Cl (**1**) in C$_7$D$_8$.*

This shows a cross peak between N–H and Y which are two bonds separated. A prominent cross peak was observed with relaxation delay of 2s and 4 scans.
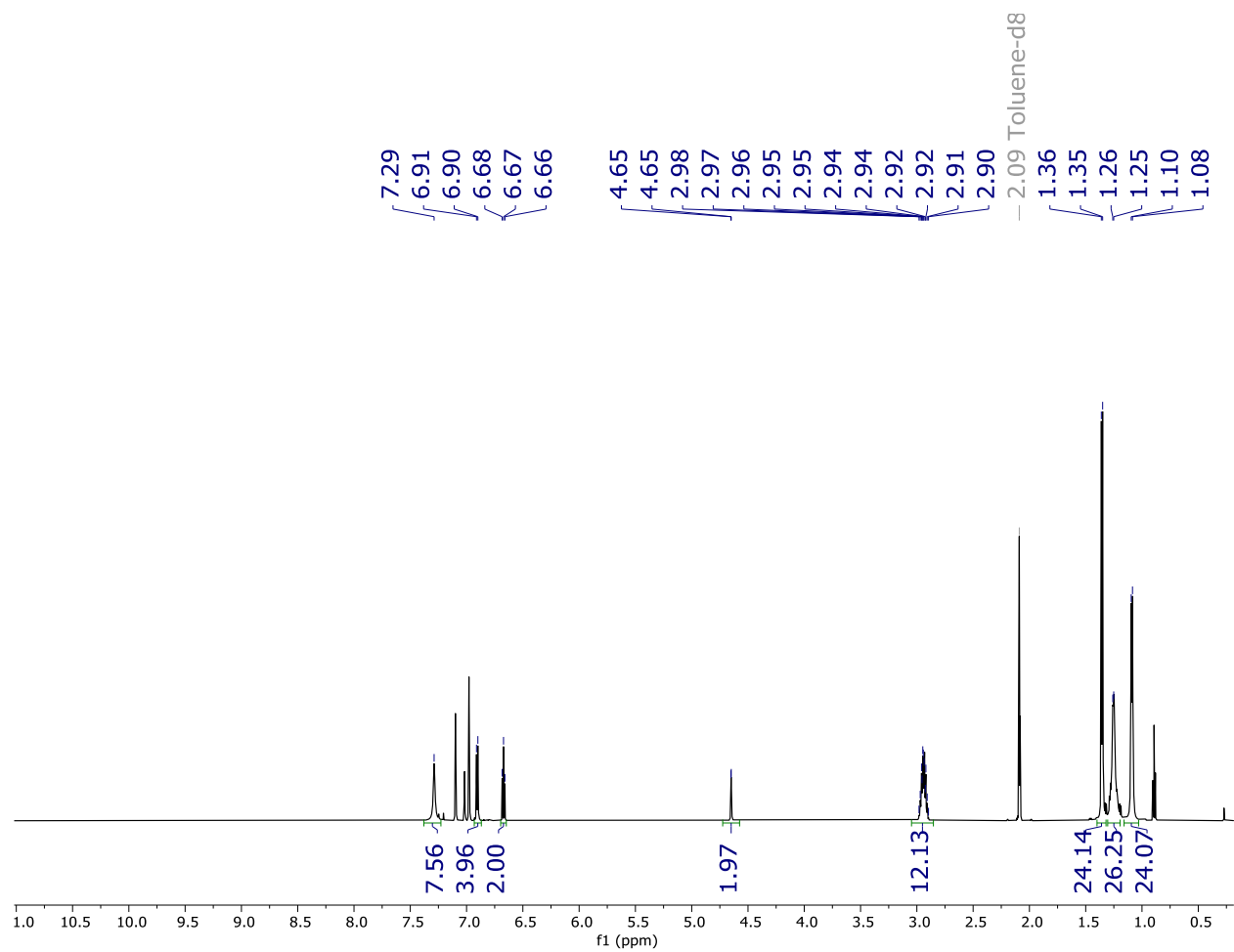
Figure S5. ^1H NMR spectrum of CN−Y(NHAr*)$_2$ (**3**) in C$_7$D$_8$.
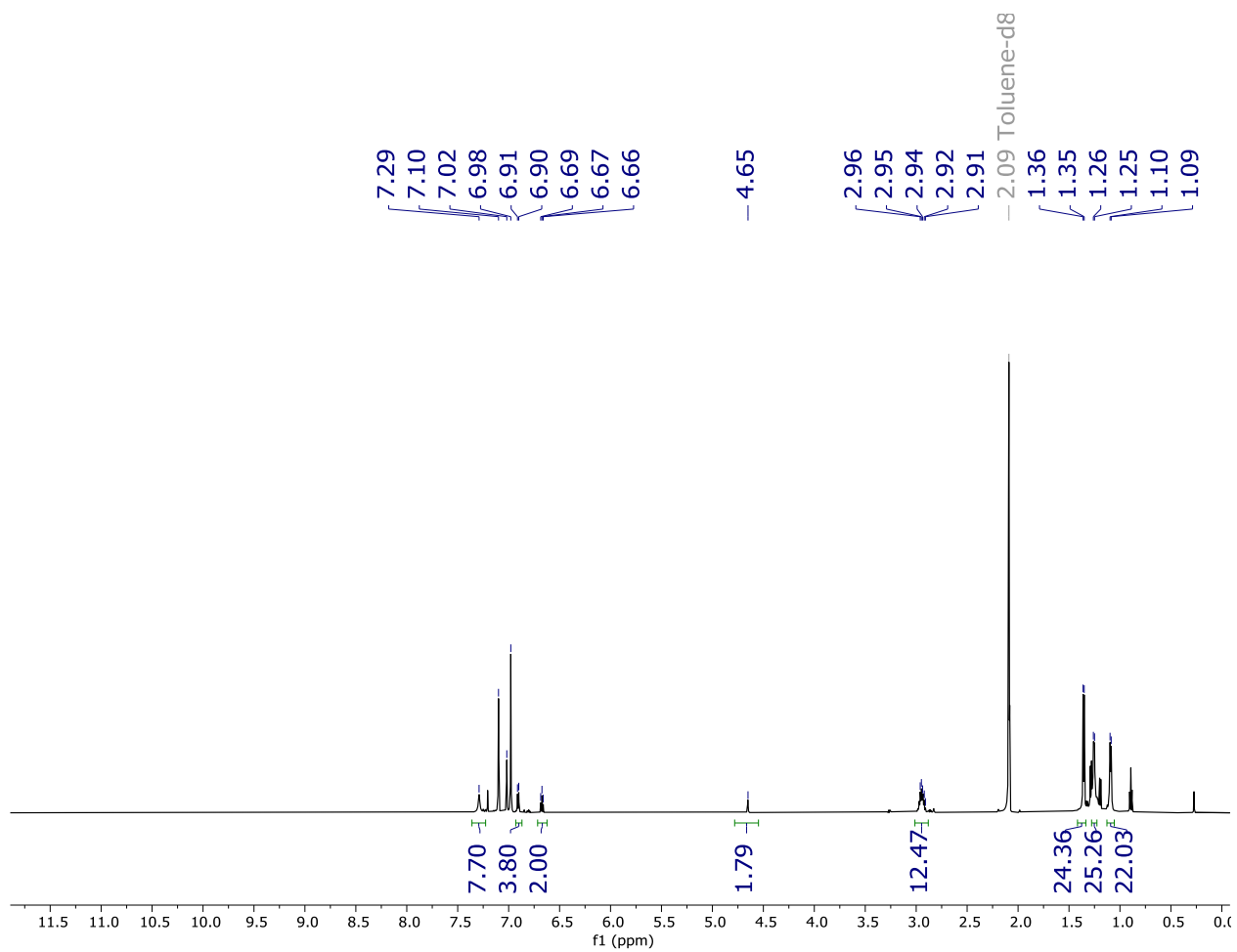
Figure S6. *^{1}H NMR spectrum of CN−Y(NHAr*)$_2$ (3a) in C$_7$D$_8$. (From NC ^{t}Bu)*
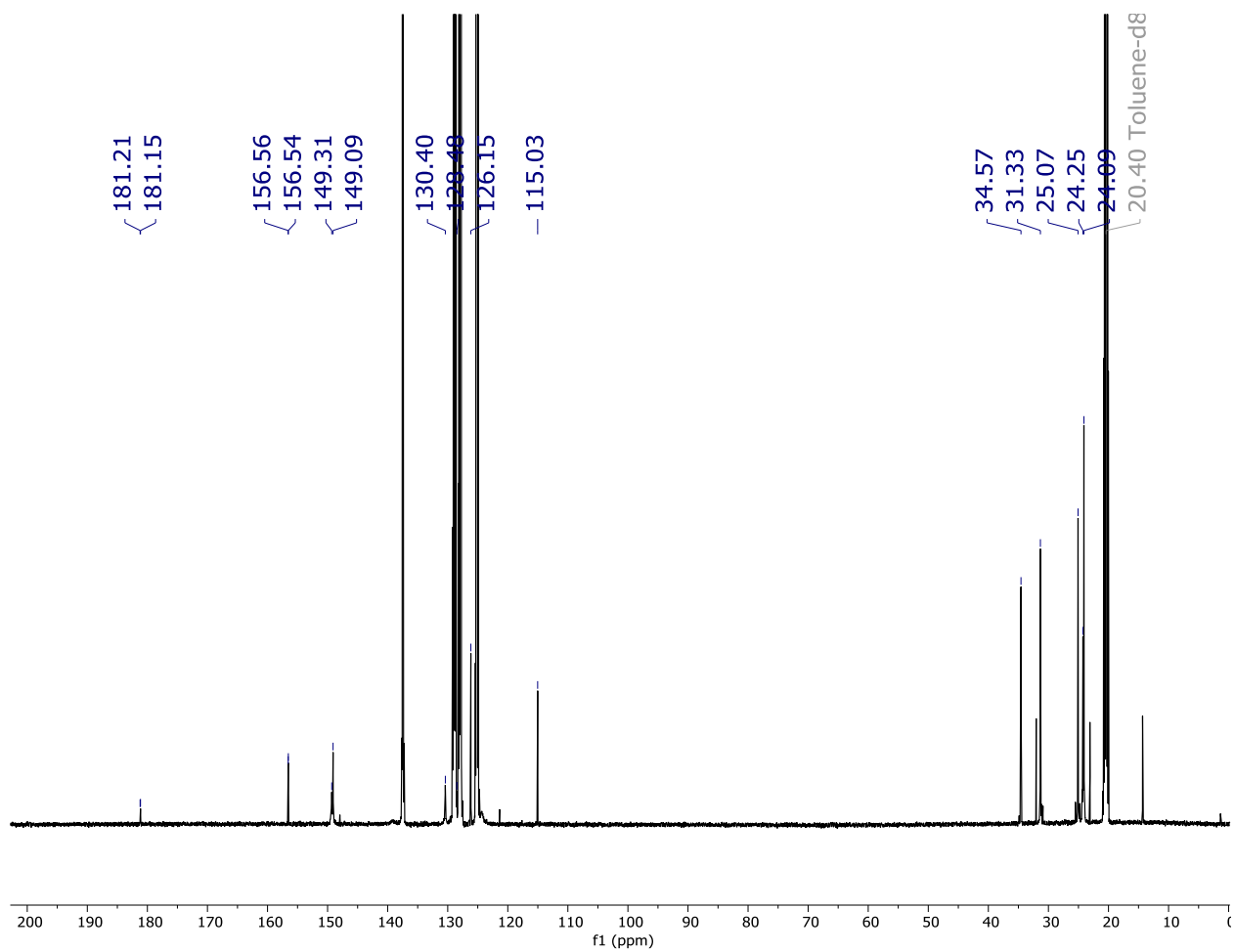
Figure S7. ^{13}C NMR spectrum of CN−Y(NHAr*)$_2$ (**3**) in C$_7$D$_8$.

Peaks: 181.21, 181.15, 156.56, 156.54, 149.31, 149.09, 130.40, 128.40, 126.15, 115.03, 34.57, 31.33, 25.07, 24.25, 21.09, 20.40 Toluene-d8
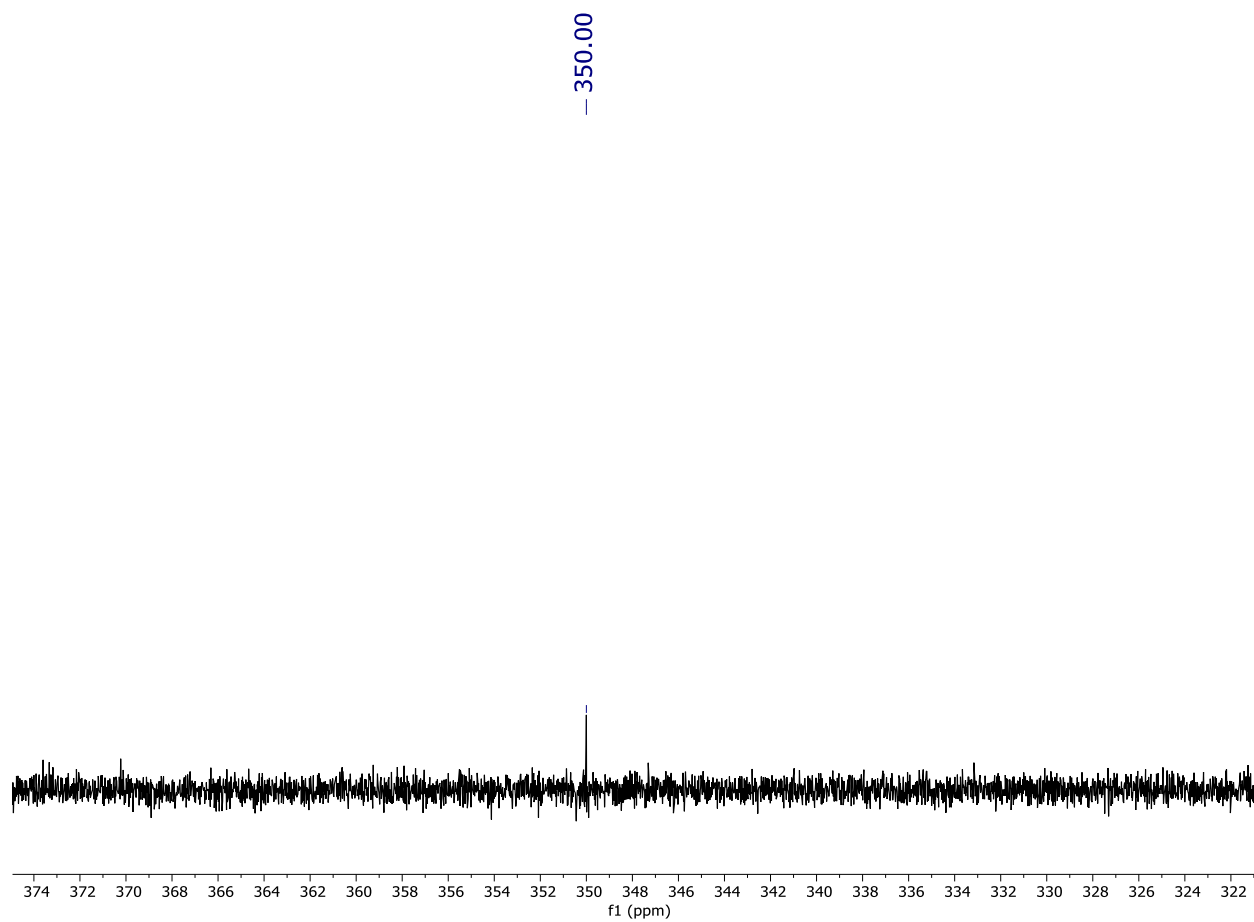
Figure S8. ^{89}Y NMR spectrum of CN–Y(NHAr*)$_2$ **(3)** (12 mM) in C$_7$D$_8$.

(This spectrum was recorded with 60 s relaxation delay and 935 scans.)
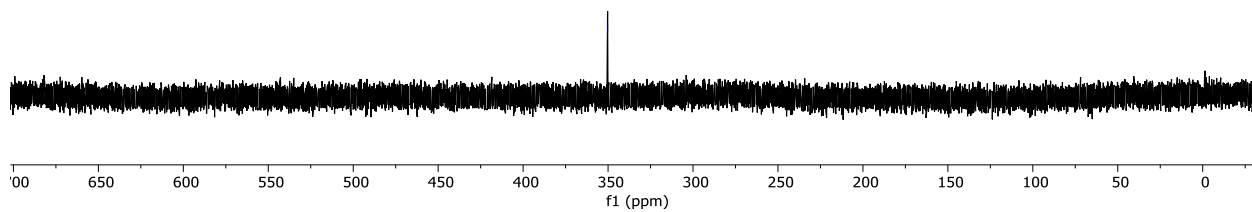
Figure S9. ^{89}Y NMR spectrum of CN–Y(NHAr*)$_2$ **(3)** (16 mM) in C$_6$D$_6$.

(This spectrum was recorded with 10 s relaxation delay and 299 scans.)
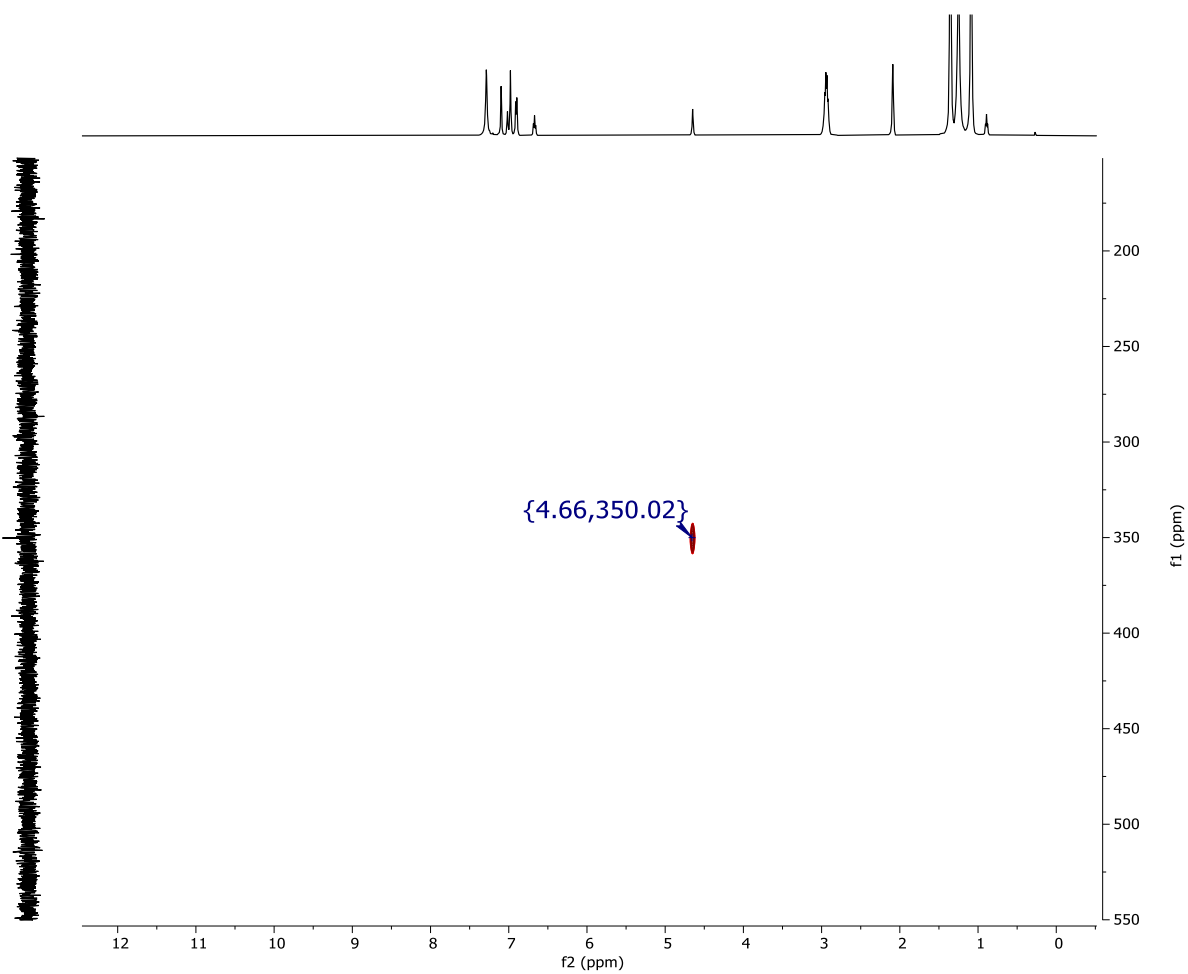
Figure S10. *HMBC for $^1H–^{89}Y$ spectrum of CN–Y(NHAr*)$_2$ (**3**) in C_7D_8.*

This shows a cross peak between N–H and Y, which are two bonds away, as expected. A prominent cross peak is observed with a relaxation delay of 2 s and 4 scans.
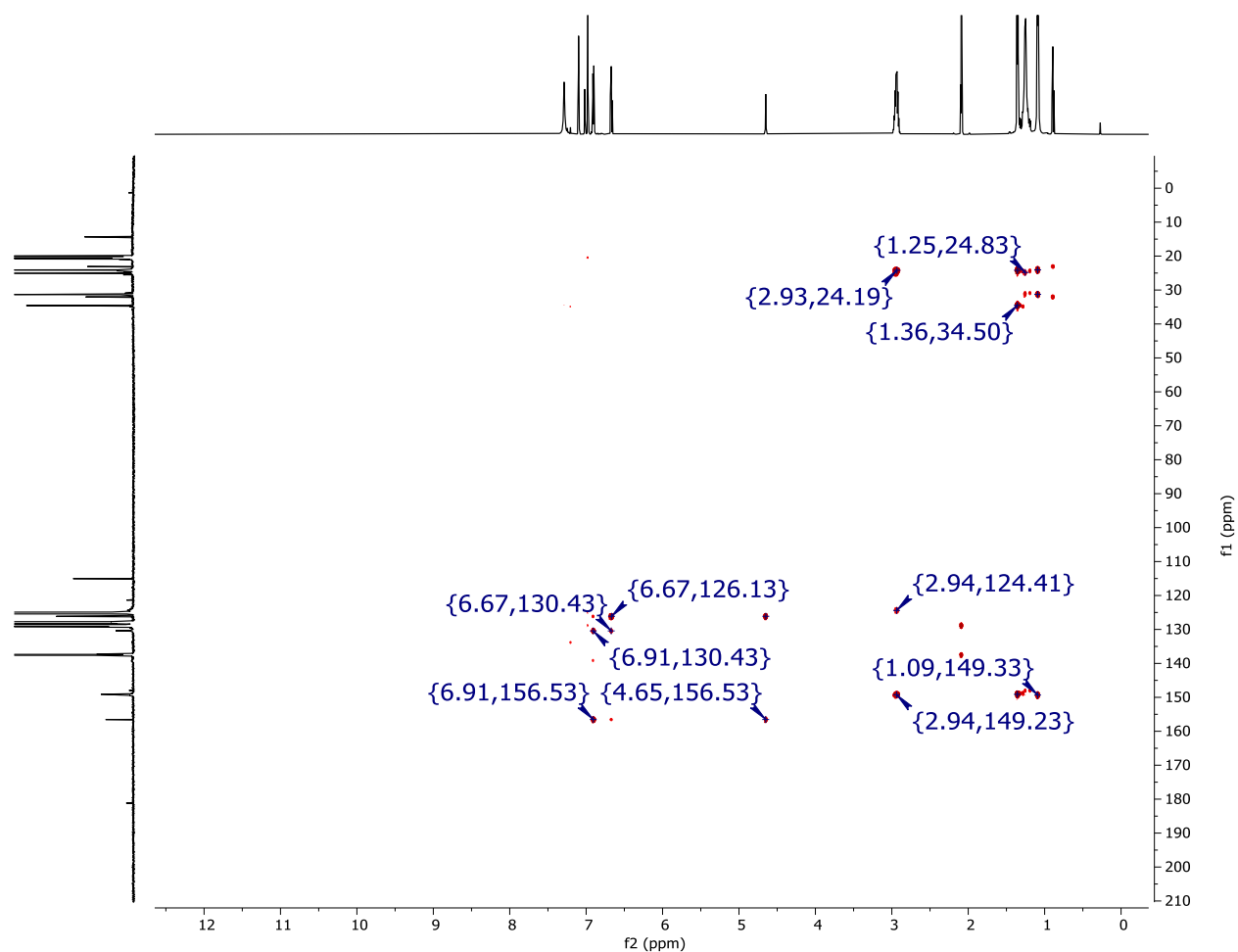
Figure S11. HMBC for $^1H-^{13}C$ spectrum of CN–Y(NHAr*)$_2$ **(3)** in C_7D_8.

The N≡C carbon does not correlate with the N–H hydrogens, which suggests that they are at least four bonds away to not appear in this HMBC spectrum. This spectrum further supports the presence of an isocyanide rather than cyanide. If it was cyanide instead of isocyanide, a cross peak might have been observed for three bond correlation, i.e., H–N–Y–CN, if the dihedral angle is not near 90°.
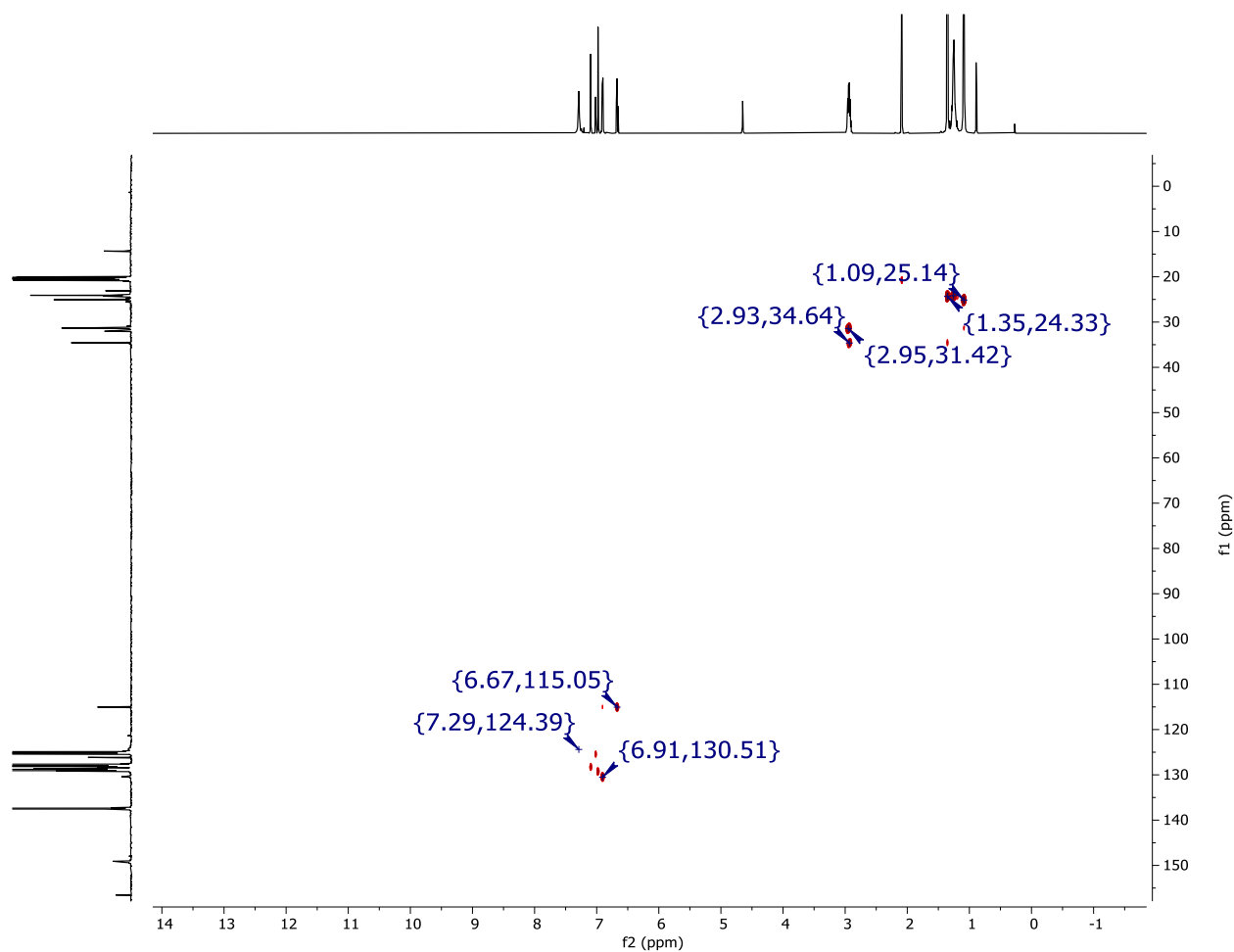
Figure S12. *HSQC for ^1H–^{13}C spectrum of CN–Y(NHAr*)$_2$ **(3)** in C$_7$D$_8$. Peak picking for residual protio-toluene omitted for clarity.*

The N≡C carbon does not correlate with any hydrogen, which shows there is no proton on the isocyanide, i.e., Y–NCH.

UV-Vis-NIR Absorption Spectrum of Y(NHAr*)$_2$ (2)

These electronic absorption spectra were recorded on a double-beam PerkinElmer 1050 spectrophotometer. The measurement was done in a 1 cm pathlength quartz cell at a ~1 mM concentration of **2**. Preparation of samples was performed in the N$_2$ glovebox using dry diethyl ether. The raw data were fit with OriginPro 9.0 software to obtain accurate maxima assuming Gaussian peak shapes.

All spectra were baseline corrected for diethyl ether and collected at ambient temperature. A broadband feature was observed at 752 nm with a molar extinction coefficient of 604.6 M^{-1} cm^{-1}. This broadband feature can be attributed to a charge transfer band in Y(NHAr*)$_2$ **2**. We were unable to locate *d-d* band which could be easily hidden under this charge transfer band. A similar broad band was observed for previously reported U(NHAr*)$_2$[8] complex at ~600 nm with molar extinction coefficient of ~1200 $M^{-1}cm^{-1}$.
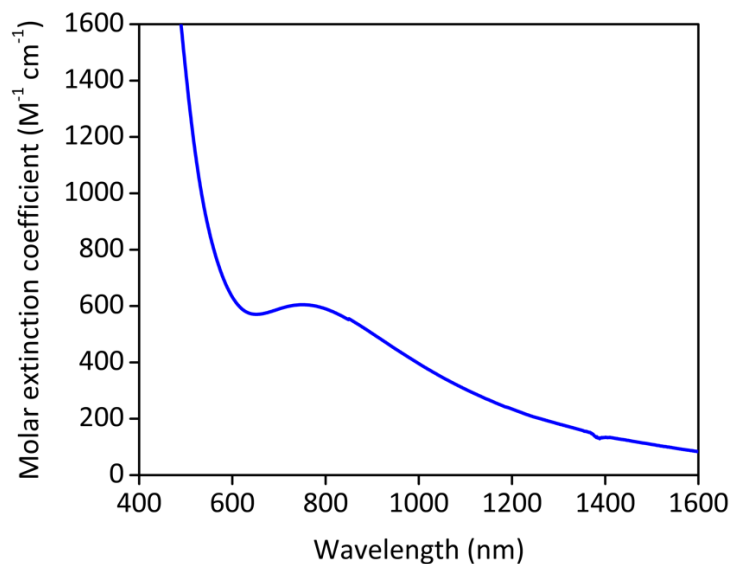
Figure S13. *UV-vis spectra at 1 mM concentration of Y(NHAr*)$_2$* **2** *in diethyl ether.*

To observe charge transfer bands low concentrations of **2** were monitored. UV-Vis spectra were collected using an Ocean Optics DH-mini UV-Vis spectrophotometer in an N$_2$ glovebox. In order to obtain molar extinction coefficients for charge transfer bands, multiple concentrations of 125 µM, 100 µM, 75 µM, 50 µM, and 25 µM solutions were prepared after dilutions.
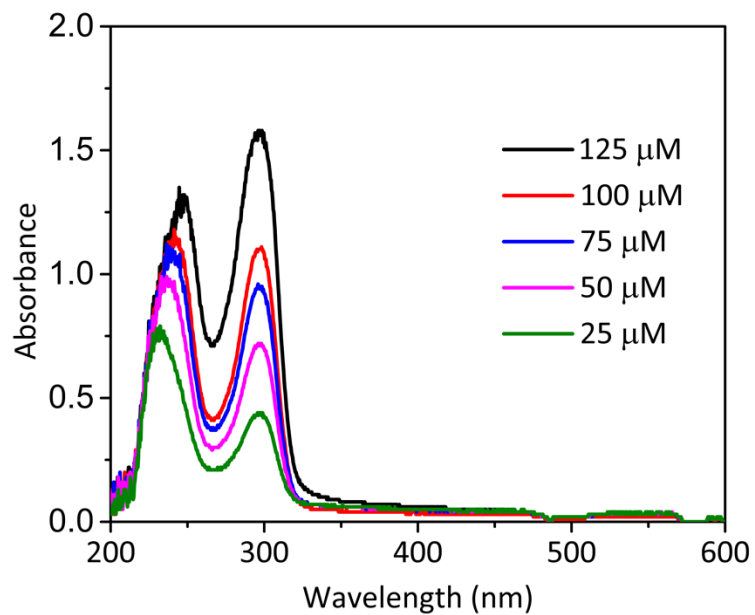
Figure S14. *UV-vis spectra at low concentrations of Y(NHAr*)₂ **2** in diethylether.*

Two absorption bands were observed between 220–350 nm. Two peak maxima are at 244 nm and 297

nm with ε = 7.3 x 10^3 M^{-1} cm^{-1} and 1.04 x 10^4 M^{-1} cm^{-1}, respectively.
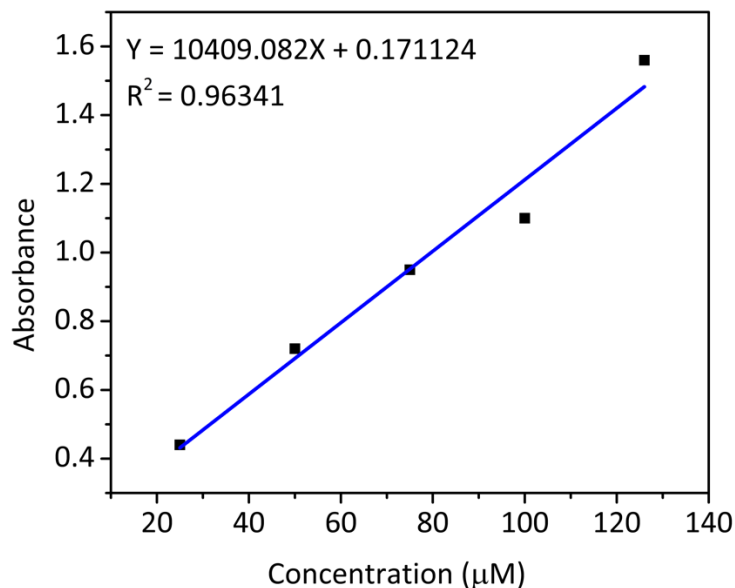
Figure S15. *Concentration vs absorbance plot to calculate molar extinction coefficient at 297 nm for Y(NHAr*)₂ **2** in diethyl ether. The slope of the line provides ε = 1.04 x 10⁴ M⁻¹ cm⁻¹ for the electronic transition occurring at 297 nm.*

Thermal Stability of Y(NHAr*)₂ (2)

The thermal stability of complex **2** at room temperature was monitored by UV-vis spectroscopy. These electronic absorption spectra were recorded on an Ocean Optics Flame DH mini spectrophotometer. The measurement was done in a 1 cm pathlength Teflon-capped quartz cell. Preparation of samples was performed in the N_2 glovebox using dry diethyl ether. The raw data were fit with OriginPro 9.0 software to obtain accurate maxima assuming Gaussian peak shapes. All spectra were baseline corrected for diethyl ether and collected at ambient temperature for up to 2 weeks.

As shown in figure S16 (Top), the decay in absorption peak at 294 nm shows a slow decomposition of the sample over time (100 h). After 100 h, there was a slight increase in the concentration, which we believe is due to a leak in the cell over the prolonged experiment time. The initial concentration was ~110 µM which was decreased to ~93 µM (85% of the initial concentration) after approximately 100 hours. First- and second-order plots between concentration and time for the decomposition rate of complex **2**

at room temperature (figure S16, bottom) under these conditions gives a very poor fit. On average, ~3% of the sample was decomposed per day.
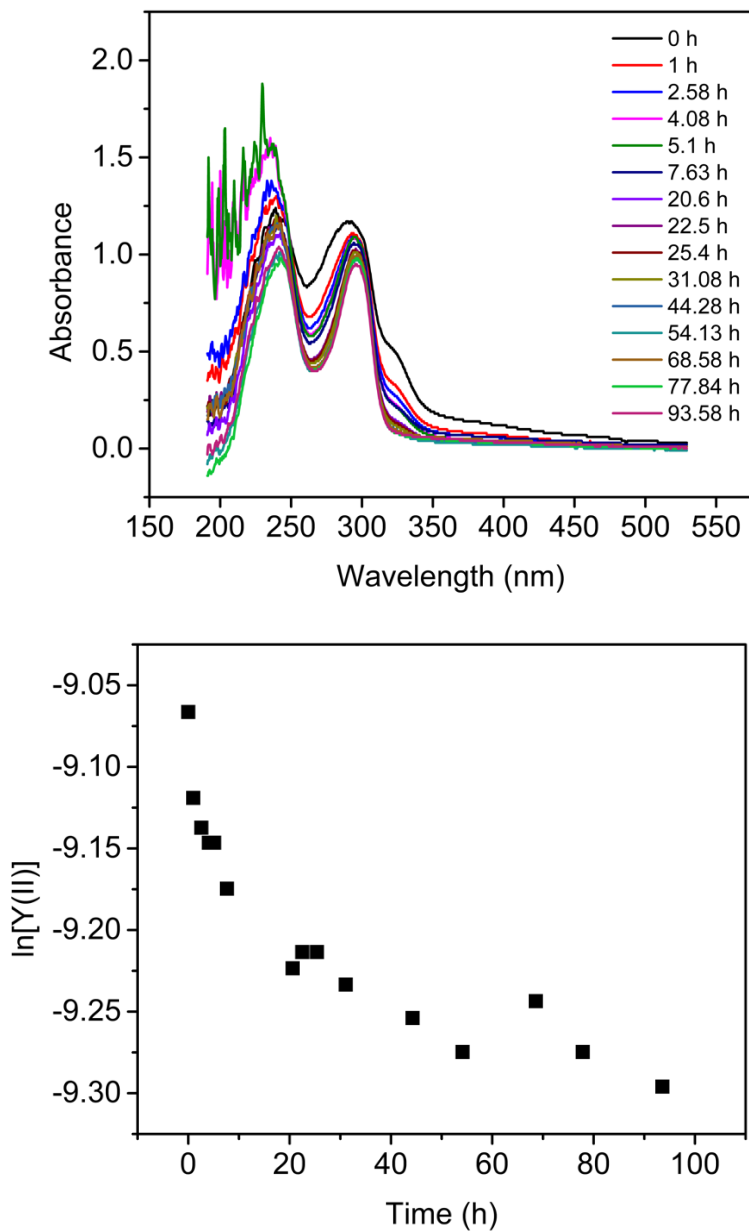
Figure S16. (Top) *Overlay of the absorption spectrum of Y(NHAr*)₂ over time. (Bottom) The logarithm of yttrium complex **2** concentration vs time plot.*

Solution-State Magnetism (Evans' Method)

Solution-state magnetic susceptibility studies were carried out on **2** using the Evans method. The resulting temperature-dependent paramagnetism was measured in 10 K intervals from 298-183 K. In a Teflon capped J-Young NMR tube 20 mM sample of **2** in toluene-d^8 and hexamethyldisiloxane was transferred with a sealed capillary tube containing 20 mM hexamethyldisiloxane in toluene-d^8 as a reference. The difference between HMDSO peak value with and without paramagnetic species was analyzed to measure effective magnetic moment of **2**.[9]
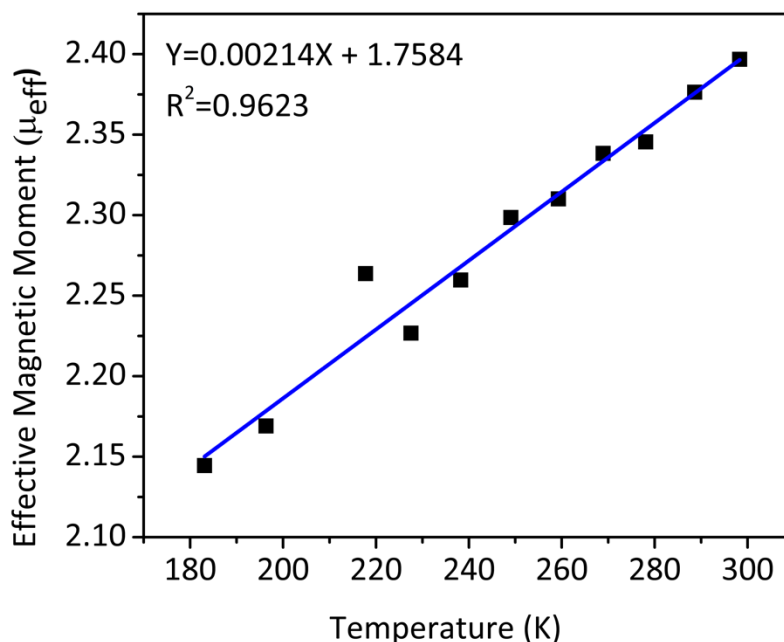
Figure S17. *Temperature dependence of solution state effective magnetic moment for complex Y(NHAr*)₂ (2).*

At room temperature the $\chi_M T$ value of **2** is 0.71 cm³ K mol^{-1} (μ_{eff} = 2.39), which decreased to 0.57 cm³ K mol^{-1} (μ_{eff} = 2.14) at 183 K as expected by the Curie law. These values are slightly higher than the spin-only magnetic moment for one electron system ($\mu_{s.o.}$ = 1.73) which can be attributed to unquenched orbital angular momentum contribution to the magnetic moment. Data points were corrected for diamagnetic contributions using Pascal's constant.[10]

24

Solid-State Magnetism (SQUID)

Direct current (dc) magnetic susceptibility measurements were carried out on a polycrystalline sample of **2** via SQUID magnetometry in applied dc magnetic fields of 0.1 T, 0.5 T, and 1.0 T between 2 and 300 K, Fig. 4 in the manuscript. The temperature dependence of the $\chi_M T$ product exhibits a gradual downturn in $\chi_M T$ with decreasing temperature indicating a deviation from the Curie-Weiss behavior expected for an ideal paramagnet. Such deviations can be a result of a) thermal depopulation of low-lying excited states, b) intermolecular through-space coupling or c) temperature-independent paramagnetism. To explain this variance from ideal behavior, the $\chi_M T$ vs. T curves were fit by freely refining the g value taking into account a weak intermolecular coupling term (zJ') alone. However, these fits yielded unrealistic high intermolecular coupling constants and precluded a satisfactorily description of the experimental values. Instead, the gradual decline in $\chi_M T$ required the consideration of a small contribution from temperature-independent paramagnetism (*TIP*, 10.400(42) − 9.212(60) x 10^{-4} cm^3 mol^{-1} (0.1 - 1.0 T)), affording a satisfying agreement with the experimental values. The inclusion of TIP and zJ' contributions gave rise to small antiferromagnetic zJ' values (−0.0890(91) - −0.1651(104) cm^{-1}) while the fitted g- and *TIP*-values remained largely unaltered. This weak intermolecular antiferromagnetic coupling is also reflected in the fitted values of the Curie-Weiss plots (1/χ_M vs. T) below 70 K, where small negative Weiss constants were found (Θ = −1.3141 - −1.2980 K). Notably, the 1/χ_M vs. *T* plots deviate from ideal Curie-Weiss behavior, indicated by the substantial positive curvatures at temperatures > 60 K for all applied dc fields. This is largely attributed to the *TIP* contribution apparent in the $\chi_M T$ vs. T curves.[2] The room temperature $\chi_M T$ value of 0.534 cm^3 K mol^{-1} at 1.0 T (0.581 cm^3 K mol^{-1} at 0.1 T, and 0.549 cm^3 K mol^{-1} at 0.5 T) is higher than the expected value of 0.375 cm^3 K mol^{-1} for the corresponding free $4d^1 5s^0$ Y(II) ion. Such discrepancy between experimental and theoretical value is not uncommon and slightly higher room temperature $\chi_M T$ values were reported for other Y(II) complexes such as [K(crypt-222)][Cp'$_3$Ln].[1] The deviation is considerably lower for **2** and closer to the expected value when subtracting the fitted temperature-

independent contributions for each field, resulting in room temperature $\chi_M T$ values of 0.318, 0.315 and 0.312 cm^3 K mol^{-1} for 0.1 T, 0.5 T and 1.0 T.

The fits of the $\chi_M T$ vs. T data (Fig. S18) engendered slightly lower g values than the expected g value of 2.0023 for an unpaired electron that is unaffected by spin-orbit coupling. Hence, the isothermal field-dependent magnetization (M vs. H) data were collected between 2 and 10 K up and at fields up to 7 T. The resulting experimental data was fit to a set of Brillouin functions to afford g values near the expected value (1.9938(19) − 2.3163(36)), which are in excellent agreement with the values attained from EPR spectroscopy.

The magnetic properties of **2** were also probed through measuring a toluene solution of **2** employing Evans' method between temperatures of 183 and 298 K, Fig. S17. Similar to the determined $\chi_M T$ values on the solid sample, a higher magnetic moment μ_{eff} = 2.39 μ_B was obtained relative to the spin-only value of 1.73 μ_B for an unpaired electron, which is likely ascribed to the aforementioned *TIP* contribution.

26
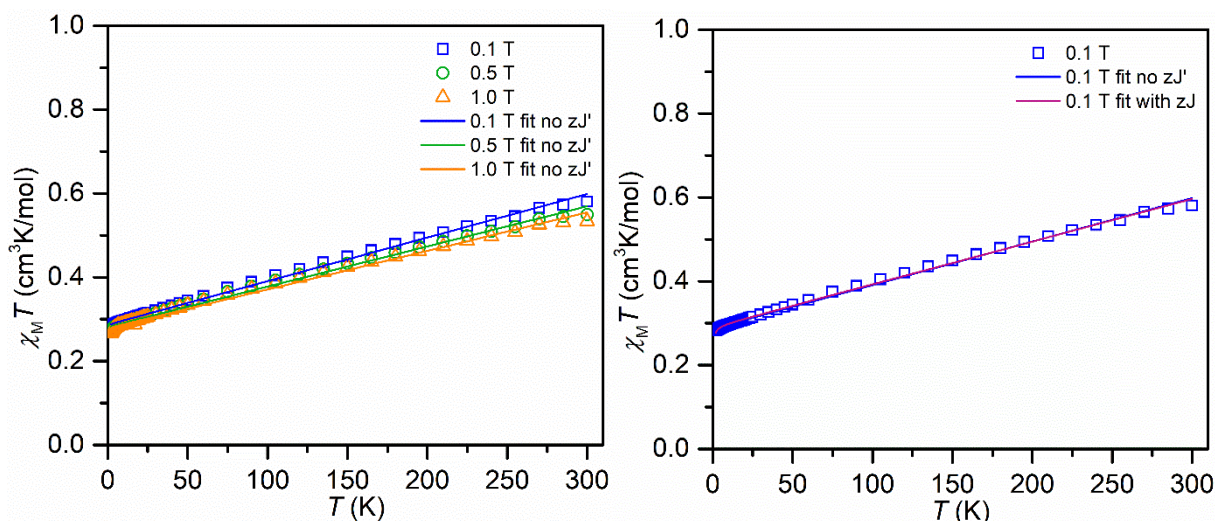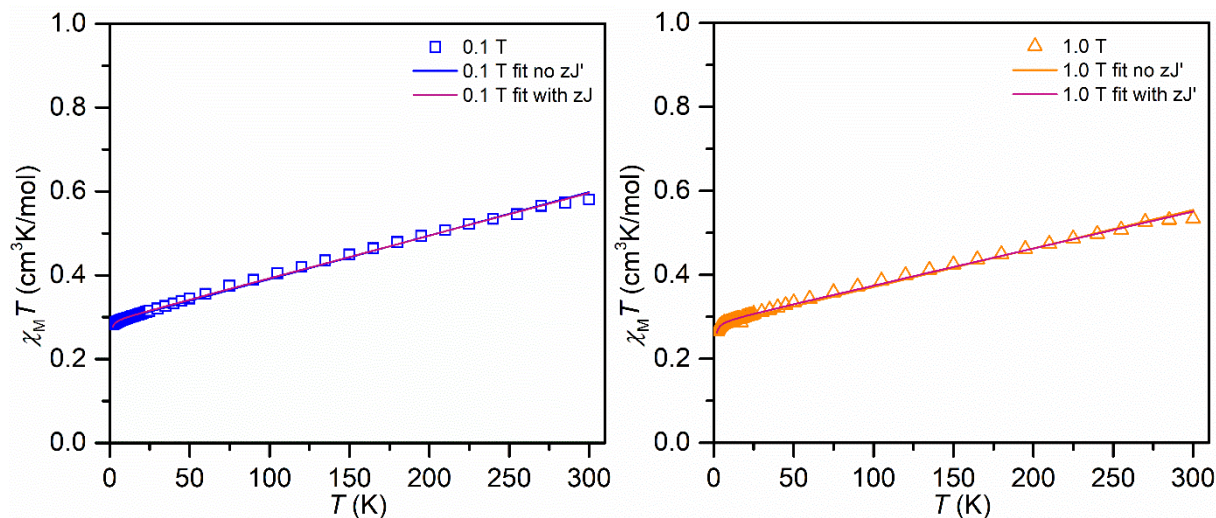
Figure S18. *Temperature dependence of the product of magnetic susceptibility and temperature, $\chi_M T$, for a restrained polycrystalline sample of Y(NHAr*)$_2$, **2**, with fits to g and TIP, and under consideration of additional zJ' terms, collected under 0.1 T (left) and 1.0 T (right) applied dc fields and at temperatures between 2 to 300 K. Fit parameters 0.1 T: g = 1.7483(12), TIP = 10.4(42) x 10^{-4}, residue = 14.1 x 10^{-4}; g = 1.7627(18), TIP = 10.400(42) x 10^{-4}, zJ' = −0.0890(91) cm^{-1} (0.1 T), residue: 8.6 x 10^{-4}. Fit parameters 1.0 T g = 1.7236(17), TIP = 9.212(60) x 10^{-4}, residue: 26.3 x 10^{-4}; g = 1.7491(19), TIP = 8.819(44) x 10^{-4}, zJ' = −0.1651(104) cm^{-1}, residue: 9.6 x 10^{-4}.*
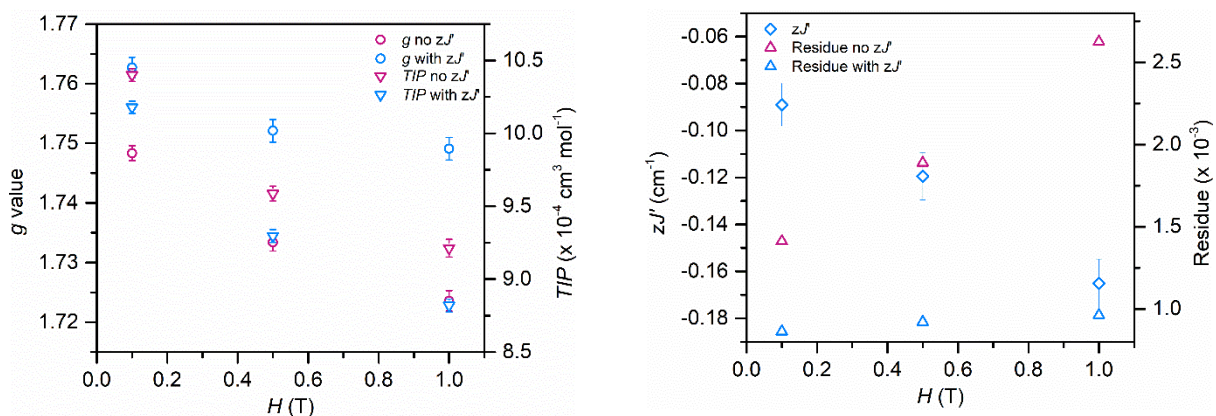
Figure S19. *Plots of the parameters employed to fit the $\chi_M T$ vs. T of Y(NHAr*)$_2$, **2**: the g and TIP values are plotted against the field (left), and the zJ' and fit residues are plotted against the field (right). In both plots, the red symbols represent the fit parameters without a zJ' contribution and the blue symbols consider a zJ' term.*
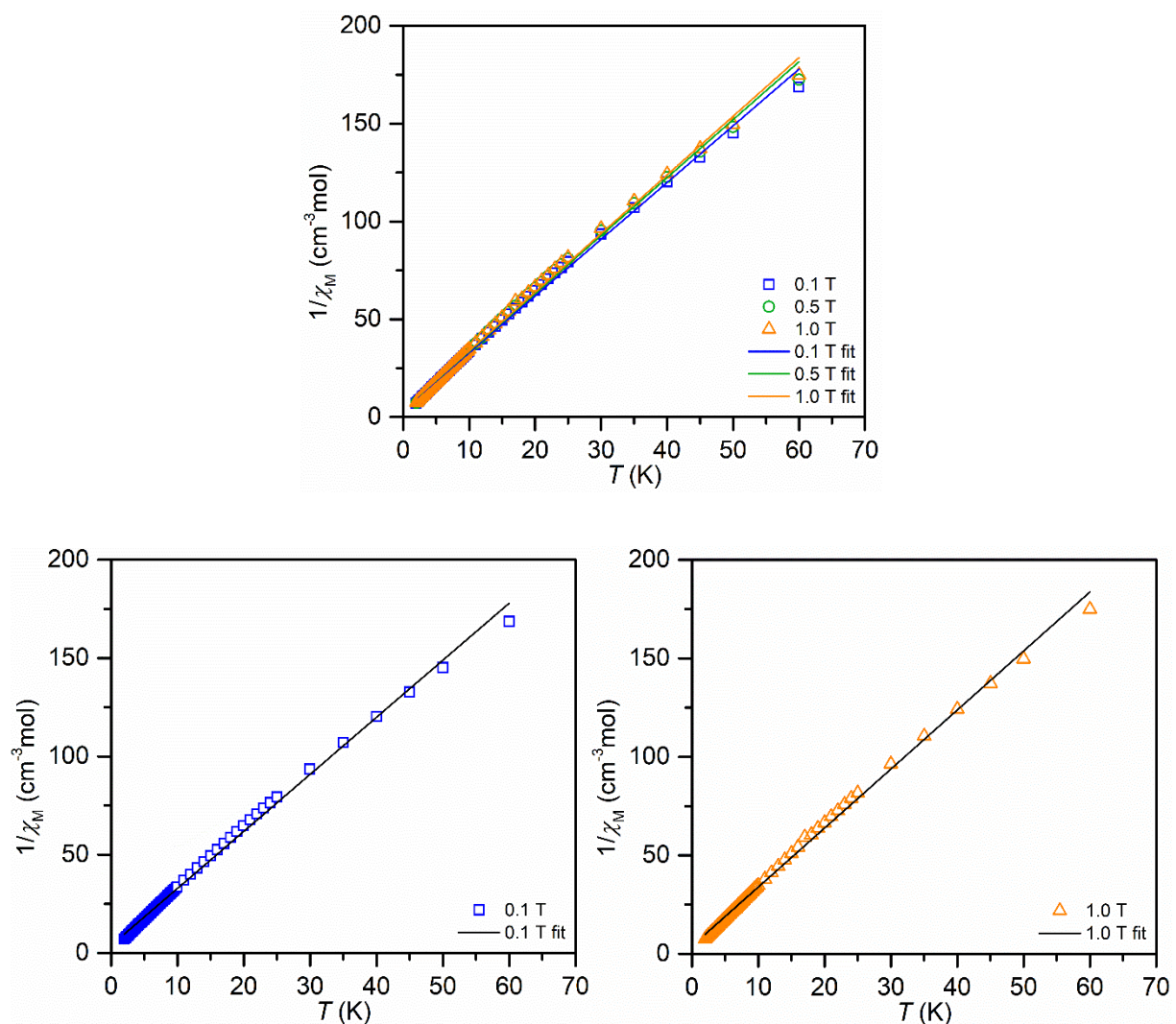
Figure S20. *Curie-Weiss plots of the inverse magnetic susceptibility (1/χ_M) versus temperature (T) for Y(NHAr*)$_2$, collected under 0.1 T, 0.5 T and 1.0 T applied dc fields and at temperatures between 2 and 300 K: superimposed spectra and corresponding fits (top), and 1/χ_M vs. T plots at 0.1 T (bottom left) and 1.0 T (bottom right). Fit parameters 0.1 T: C = 0.345(22) cm^3 K mol^{-1}, Θ = −1.314 K. Fit parameters 1.0 T: C = 0.334(22) cm^3 K mol^{-1}, Θ = −1.298 K.*
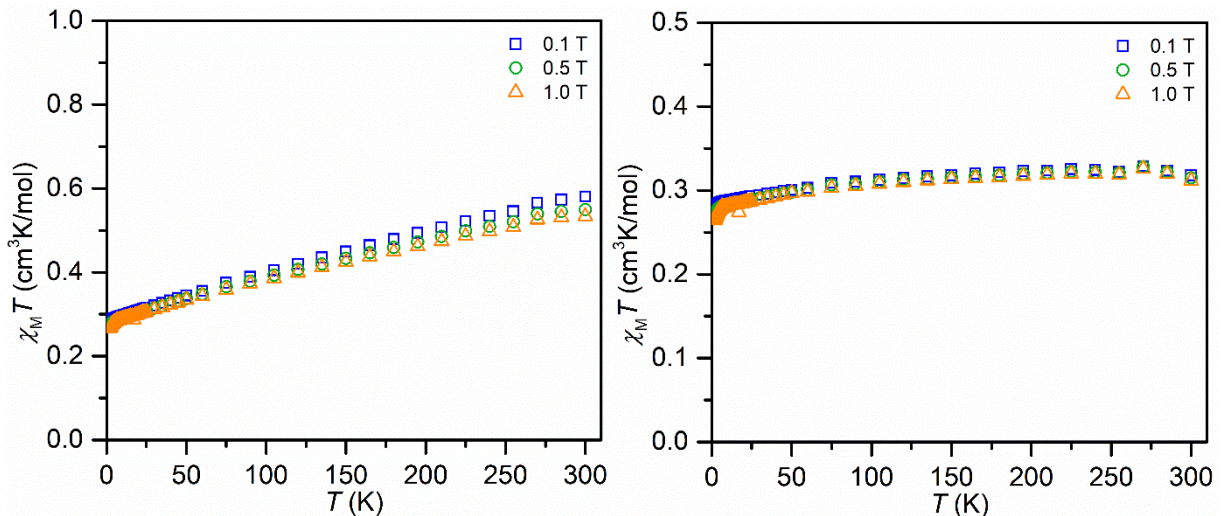
Figure S21. *Variable-temperature dc magnetic susceptibility data for a restrained polycrystalline sample of Y(NHAr*)$_2$, **2**, collected under 0.1 T, 0.5 T and 1.0 T applied dc fields and at temperatures from 2 to 300 K (left) and $\chi_M T$ vs. T curves with subtracted TIP contributions (right).*
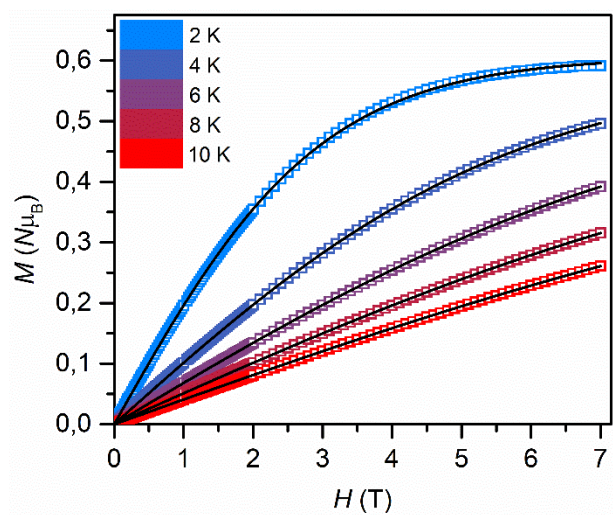
Figure S22. *Variable temperature M(H) curves for **2** collected from 0 to 7 T. The black lines represent fits to the Brillouin function for each temperature. Fit parameters: 2 K: g = 1.9938(19), N = 0.6087(8); 4 K: g = 2.0491(8), N = 0.5804(4); 6 K: g = 2.1229(14), N = 0.5417(6); 8 K: g = 2.2117(23), N = 0.4987(9); 10 K: g = 2.3163(36), N = 0.4534(13).*

FT-IR Spectroscopy

IR Spectra were recorded using Varian 3100 FT-IR spectrometer with a spectral resolution of 2 cm^{-1} using a CaF$_2$ air-free cell. Sample preparation was done in the glove box under an N$_2$ atmosphere and sealed with Teflon caps before measurements. All spectra were recorded in the solution phase using dry *n*-hexane as solvent. The IR transmittance spectra were collected at 298 K and baseline corrected. The v_{CN} stretch for tert-butyl isocyanide is 2127 cm^{-1} in *n*-hexane matches with literature reported value.[11] Since complex **3** can also be synthesized from trimethylacetonitrile, we recoded IR spectrum (2237 cm^{-1}) for comparison. The v_{CN} stretch for complex **3** is 2053 cm^{-1} is lower in energy than both starting materials and is also in agreement with previously reported metal isocyanides.
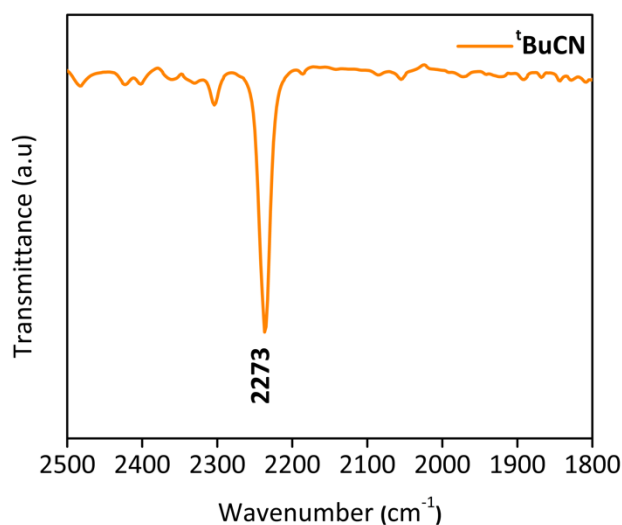
Figure S23. *IR spectrum for trimethylacetonitrile in n-hexane.*
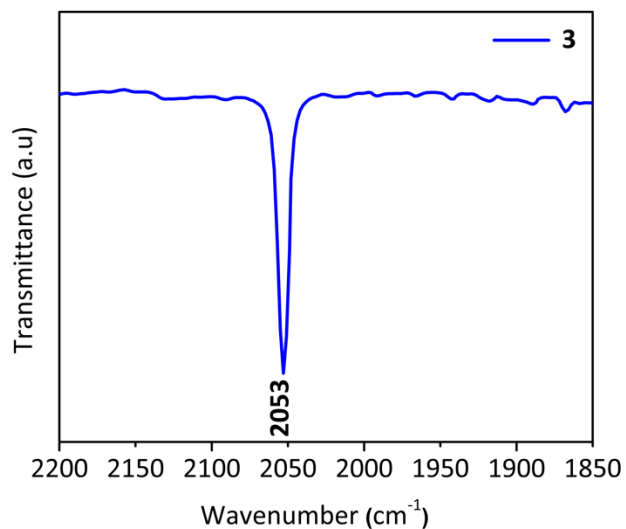
Figure S24. *IR spectrum for complex Y(NHAr*)$_2$NC **3** (~5 μM) in n-hexane.*

EPR Spectroscopy

EPR spectra were collected on a Bruker E-680X spectrometer operating at X-band and fitted with a Bruker SHQ-E cavity. For experiments done over the range of 130 – 330 K, a Bruker B-VT-2000 temperature control system was used. Experiments done at 20 – 80 K made use of an Oxford ESR-900 cryostat and an ITC – 301 temperature controller. The magnetic field was calibrated using weak pitch as standard and the microwave frequency was monitored with an EIP – 25B counter. Spectral simulations were done using EasySpin 5.2.35[12] and fit using the "fminsearch" function of MATLAB R2020A. The quality of the fits was judged by calculating a normalized $\chi 2$ value based on using 1% of the maximum spectral amplitude as the standard deviation. For the fits, the normalized $\chi 2$ values were 0.9 (60 K) and 0.4 (295 K).

Samples were prepared for EPR spectroscopy in the dry box using dry degassed toluene. The samples were loaded as a solution into a quartz EPR tube and sealed under vacuum.

Cyclic Voltammetry

Cyclic voltammetry was recorded using a PGSTAT204 potentiostat from Metrohm with a glassy carbon working electrode, platinum wire pseudoreference electrode, and platinum wire as a counter electrode. All measurements were in the glovebox under argon atmosphere. Y(NHAr*)$_2$ **2** (1.5 mM) was dissolved in diethyl ether with [NBu$_4$]$^+$[B(3,5-(CF$_3$)$_2$C$_6$H$_3$)$_4$]$^-$ (100 mM) as supporting electrolyte. Cyclic voltammetry of ferrocene was performed six times to get standard deviation in potential shifts. All voltammograms were externally referenced to ferrocene with same electrolyte concentration. All measurements were done in triplicate to get an average value of half-cell potential with scan rates of 50 mV/s and 100 mV/s (*vide infra*).
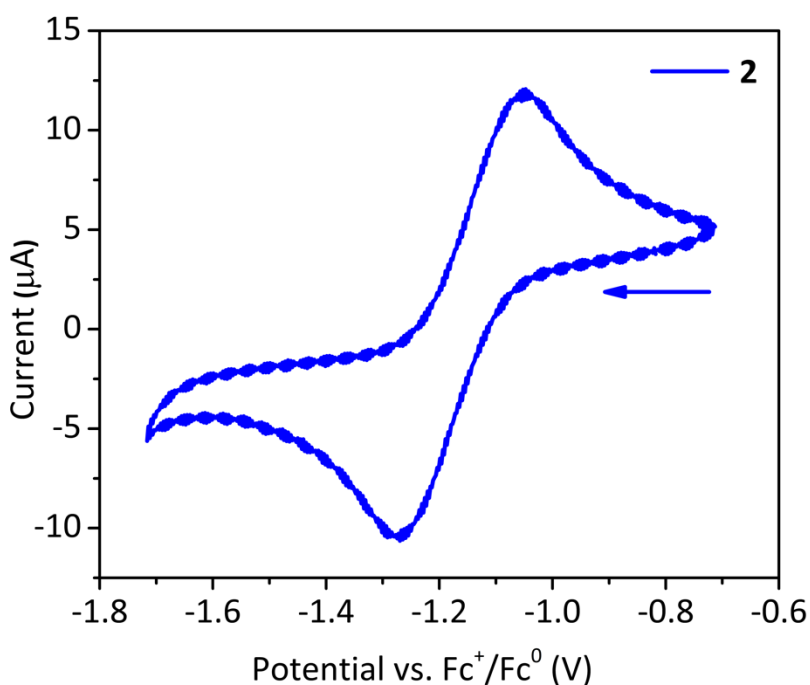
Figure S25. *Cyclic Voltammogram of **2** in Et$_2$O with [NBu$_4$]$^+$[B(3,5-(CF$_3$)$_2$C$_6$H$_3$)$_4$]$^-$ (100 mM) as supporting electrolyte and Fc$^{+/0}$ as 0 V. This voltammogram was scanned in negative direction with 100 mV/s scan rate.*

A reproducible quasi-reversible feature was observed at −1.16 ± 0.01 V vs. Fc$^+$/Fc^0 on the time scale of the electrochemical experiments assigned to the 0/+1 redox couple.
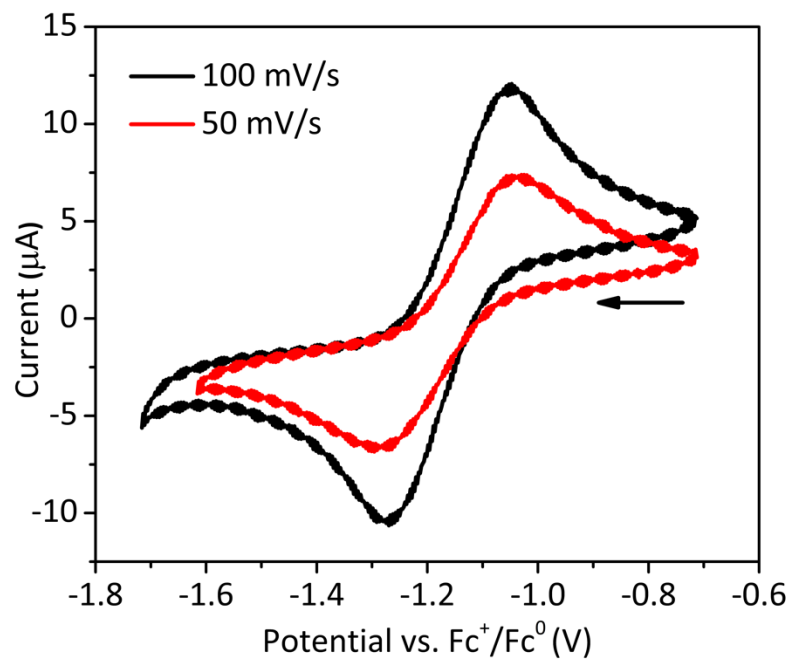
Figure S26. *Overlay plot for scan rates 100 mV/s (black) and 50 mV/s (red).*

Table S1. *Summarized results from scan rate measurements to study reversibility of 0/+1 redox couple.*

Scan	100 mV/s	50 mV/s
E_c-E_a	0.22	0.27
i_c/i_a	1.09	1.08
$i_p/\sqrt{\text{(scan rate)}}$	36.8	33.1

Single Crystal X-ray Diffraction
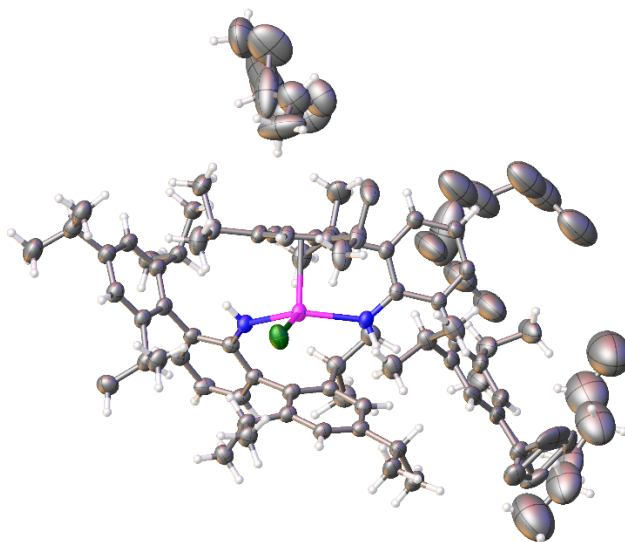
Figure S27. *Structure of Y(NHAr*)₂Cl (**1**) from X-ray diffraction recrystallized from n-hexane. Thermal ellipsoids of Y(NHAr*)₂Cl (**1**) are drawn with 50% probability level. Pink, green, blue, grey, and white ellipsoids represent yttrium, chlorine, nitrogen, carbon, and hydrogen atoms respectively. There are two disordered molecules of n-hexane in lattice per molecule of **1**.*
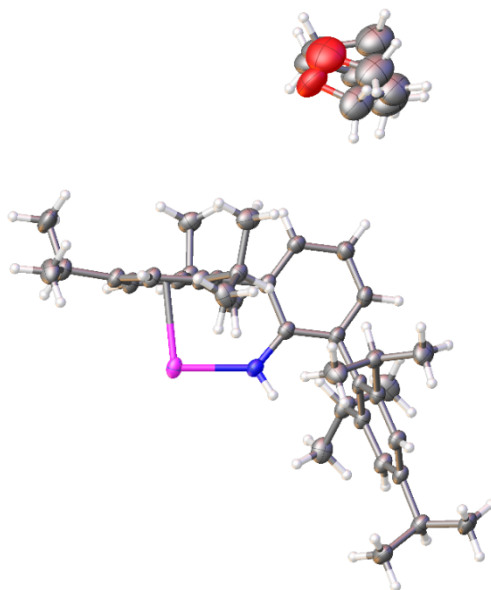
Figure S28. *Asymmetric unit of Y(NHAr*)₂ (**2**) recrystallized from n-hexane. Thermal ellipsoids of Y(NHAr*)₂ (**2**) are drawn with 50% probability level. There is one molecule of disordered THF in lattice per molecule. Pink, blue, red, grey, and white spheres represent yttrium, nitrogen, oxygen, carbon, and hydrogen atoms, respectively.*
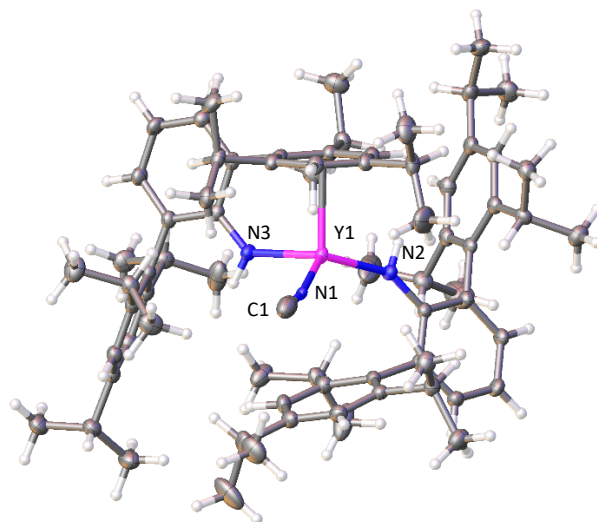
Figure S29*. Structure of CN–Y(NHAr*)₂ (**3**) recrystallized from n-hexane. Thermal ellipsoids of CN–Y(NHAr*)₂ (**3**) are drawn with 50% probability level. Pink, blue, grey, and white spheres represent yttrium, nitrogen, carbon, and hydrogen atoms, respectively.*

Figure S29 shows the structure obtained from X-ray diffraction. Along with structure the presence of CN–Y(NHAr*)₂ is reasoned by using the ^{89}Y–^{13}C coupling constant in the text. We tried to solve the structure by exchanging positions of C1 to N1 and N1 to C1. Analysis of theoretical cyanide structure gave us poor refinement values R_1 = 4.37 and wR_2 = 10.61 with more realistic thermal displacement values.

Table S2. *Thermal parameters for carbon and nitrogen atoms in CN–Y(NHAr*)₂ (**3**) vs CN–Y(NHAr*)₂ crystal structure.*

		C	N
CN–Y(NHAr*)₂	U11	0.03700	0.02170
	U22	0.04300	0.03470
	U33	0.03890	0.02610
NC–Y(NHAr*)₂	U11	0.01068	0.05490
	U22	0.00373	0.02060
	U33	0.02139	0.02495
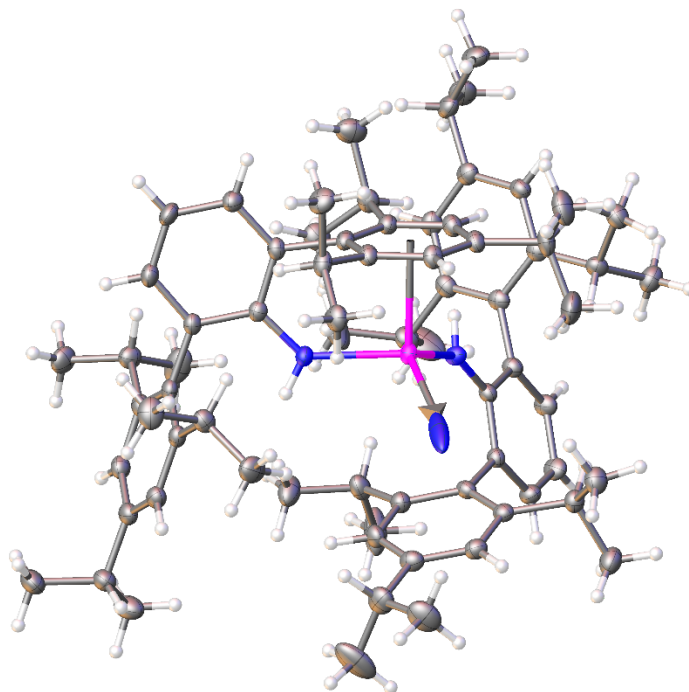
Figure S30. *Structure of NC–Y(NHAr*)₂. The CN goes to non-positive definite in the structure. Thermal ellipsoids of NC–Y(NHAr*)₂ are drawn with 50% probability level. Pink, blue, grey, and white spheres represent yttrium, nitrogen, carbon, and hydrogen atoms, respectively.*

Table S3. *Metric data from the crystal structures of Y(NHAr*)₂Cl (1), Y(NHAr*)₂ (2), and Y(NHAr*)₂NC (3). All distances are in $\mathring{A}$ and angles are in (˚).*

Complex	Y(NHAr*)₂Cl (**1**)	Y(NHAr*)₂ (**2**)	Y(NHAr*)₂NC (**3**)
Y–N	2.249(2) 2.213(2)	2.2628(7)	2.2206(17) 2.2205(17) 2.3481(18) Y1–N1
Y–Cl	2.5071(8)		
N–C$_1$			1.039(4)
Y–N–C$_{ipso}$	131.5(2) 144.2(2)	130.24(13)	145.40(15) 133.20(14)
N–Y–N	133.76(1)	102.37(9)	112.33(7) N3–Y1–N2 106.92(6) N3–Y1–N1 126.54(6) N2–Y1–N1
N–Y–Cl	104.41(7) 107.70(1)		
A$_{rcent}$–Y–N	94.98(7) 101.99(7)	95.91(4) 112.84(4)	93.70(5) 106.63(5)
Y–N–C$_{terminal}$			170.38(19)
Y-Ar$_{Cent}$	2.495(1)	2.46770(8)	2.5178(2)
Cent–Y–Cent		133.87(1)	

Y–C_{Ar}	2.781(3), 2.821(3), 2.871(3), 2.921(3), 2.903(3), 2.868(3)	2.729(2), 2.787(2), 2.953(2), 2.802(2), 3.013(2), 2.766(2)	2.800(2), 2.893(2), 2.939(2), 2.958(2), 2.880(2), 2.827(2)
η^6-C_{Ar}–C_{Ar}	1.416(5), 1.423(4), 1.400(5), 1.400(5), 1.386(5), 1.388(4)	1.444(3), 1.407(3), 1.409(3), 1.392(3), 1.418(3), 1.412(3)	1.424(3), 1.413(3), 1.402(3), 1.402(3), 1.391(3), 1.403(3)
Average C_{Ar}–C_{Ar} bond	1.402(5)	1.413(3)	1.406(3)

Table S4. *Crystallographic data and structural refinement of Y(NHAr*)$_2$Cl (**1**), Y(NHAr*)$_2$ (**2**), and*

Y(NHAr)$_2$NC (**3**).*

Complex number	1	2	3
CCDC number			
Empirical formula	$C_{84}H_{125}ClN_2Y$	$C_{76}H_{108}N_2OY$	$C_{73}H_{100}N_3Y$
Formula weight	1287.21	1154.55	1108.46
Temperature/K	99.99(10)	100.00(10)	100.00(10)
Crystal system	monoclinic	monoclinic	monoclinic
Space group	C2/c	C2/c	P2$_1$/n
a/Å	39.6030(5)	18.0163(3)	13.82181(13)
b/Å	16.4949(2)	17.0386(3)	28.6811(3)
c/Å	25.0473(3)	22.7773(4)	17.11754(15)
α/°	90	90	90
β/°	91.0170(10)	106.062(2)	106.3762(9)
γ/°	90	90	90
Volume/Å^3	16359.5(3)	6719.1(2)	6510.53(11)
Z	8	4	4
ρ_{calc}g/cm^3	1.045	1.141	1.131
μ/mm^{-1}	1.590	1.539	1.563
F(000)	5592.0	2500.0	2392.0
Crystal size/mm^3	0.196 × 0.12 × 0.101	0.076 × 0.059 × 0.024	0.087 × 0.07 × 0.039
Radiation	Cu Kα (λ = 1.54178)	Cu Kα (λ = 1.54184)	Cu Kα (λ = 1.54184)
2Θ range for data collection/°	5.804 to 154.574	7.28 to 153.926	6.202 to 154.464
Index ranges	-48 ≤ h ≤ 40, -20 ≤ k ≤ 15, -28 ≤ l ≤ 31	-22 ≤ h ≤ 21, -20 ≤ k ≤ 19, -27 ≤ l ≤ 27	-16 ≤ h ≤ 17, -33 ≤ k ≤ 36, -21 ≤ l ≤ 11
Reflections collected	59902	23782	50292
Independent reflections	15940 [R_{int} = 0.0751, R_{sigma} = 0.0692]	6674 [R_{int} = 0.0295, R_{sigma} = 0.0278]	12920 [R_{int} = 0.0433, R_{sigma} = 0.0388]
Data/restraints/parameters	15940/287/1044	6674/198/427	12920/0/726
Goodness-of-fit on F^2	1.032	1.033	1.035
Final R indexes [I>=2σ (I)]	R_1 = 0.0598, wR_2 = 0.1564	R_1 = 0.0417, wR_2 = 0.1130	R_1 = 0.0411, wR_2 = 0.0911
Final R indexes [all data]	R_1 = 0.0765, wR_2 = 0.1727	R_1 = 0.0446, wR_2 = 0.1150	R_1 = 0.0508, wR_2 = 0.0951
Largest diff. peak/hole / e Å^{-3}	0.80/-0.75	0.59/-0.70	0.61/-0.55

DFT Calculations

DFT calculations were carried out using Gaussian 16 (B01).[13] The starting coordinates for the geometry

optimisations were taken from the structure found from X-ray diffraction. Geometry optimisation and

frequency calculations were performed using the B3LYP functional and def2-SV(P)[14] basis set on all atoms

with the ECP28MDF[15] pseudopotential on the yttrium atom with Grimme's dispersion correction GD3.[16,17] The NBO calculations were carried out using NBO7.

DFT calculations were performed to understand the bonding interactions between yttrium and ligand system in complex **2**. In comparison to the initial structure obtained crystallographically, the DFT calculations provided a consistent structure to experimentally obtained structure (shown in Fig. S28 and Table S5).
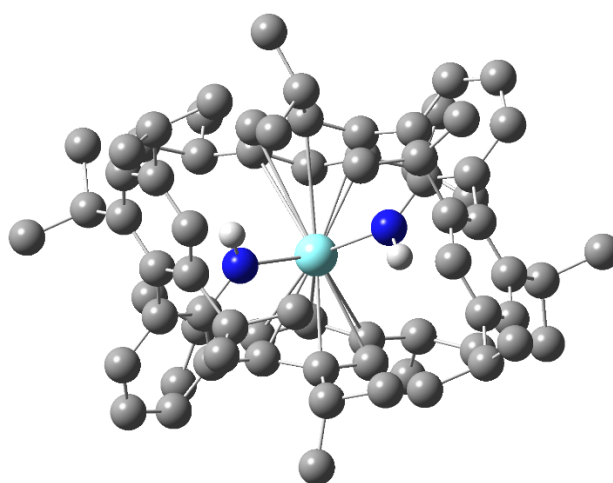

Figure S31. *Optimised structure of Y(NHAr*)$_2$ (**2**) using B3LYP/def2-SV(P). All hydrogens are removed for clarity except N—H hydrogens. Light blue, blue, grey, and white spheres represent yttrium, nitrogen, carbon, and hydrogen atoms, respectively.*

Table S5. *Structural comparisons between crystallographically obtained geometry of **2** and optimised geometry using DFT calculations. Shown here are some characteristic lengths (Å) and angles (˚).*

Atoms	Distance (Å)/Angle (°) Experimental	Distance (Å)/Angle (°) Calculated
Y–N	2.2628(7)	2.277
Y-Ar$_{Cent}$	2.46770(8)	2.465
Cent–Y–Cent	133.87(1)	137.24
Y–N–C$_{ipso}$	130.24(13)	130.11
A$_{rcent}$–Y–N	95.91(4) 112.84(4)	95.82 110.85
Average C$_{Ar}$–C$_{Ar}$ bond	1.413(3)	1.419

The HOMO and LUMO (Fig. S32) of Y(NHAr*)$_2$ (**2**) encompassing yttrium and arene rings suggest the movement of unpaired electron density throughout the metal-ligand backbone. Further Mulliken spin

density confirmed the delocalized electron density on ligand consistent with hyperfine splitting obtained

from EPR spectroscopy. The isotopic hyperfine splitting constant A_{iso} (40.2 MHz) is significantly smaller

than previously reported yttrium radical complexes suggesting that some of the electron density is

delocalized on the NHAr* ligand backbone.
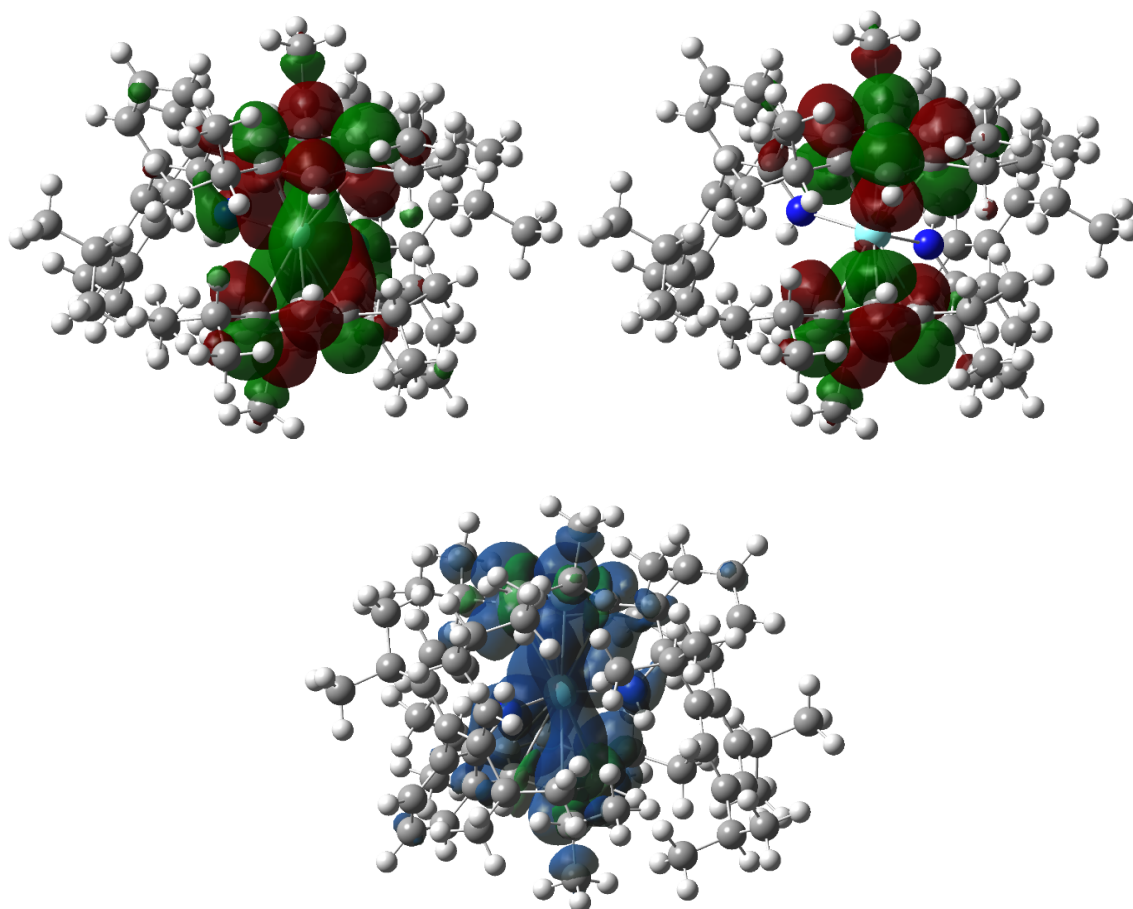
Figure S32. *HOMO (top, left), LUMO (top, right), and spin density map (bottom) of Y(NHAr*)$_2$ (**2**). Light blue, blue, grey, and white spheres represent yttrium, nitrogen, carbon, and hydrogen atoms, respectively.*

The yttrium isocyanide Y(NHAr*)$_2$NC (**3**) and hypothetical yttrium cyanide Y(NHAr*)$_2$CN (**3'**) were also

studied computationally. The structure obtained from DFT calculations (Fig. S33) was consistent with the

experimental results from X-ray diffraction (Table S6). The NBO analysis showed triple bonds between

terminal N–C bond with a lone pair residing on the carbon atom further proves presence of isocyanide over cyanide linkage.

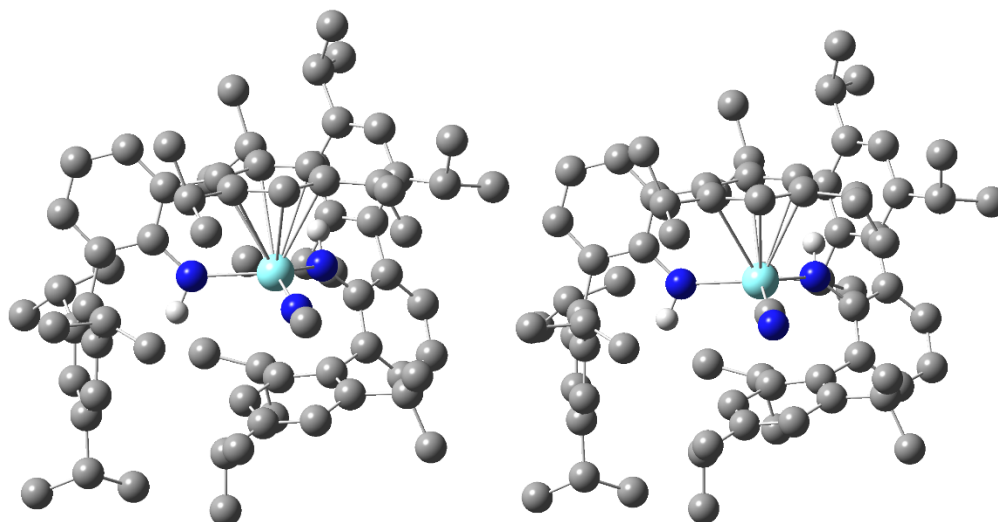**Figure S33.** Optimised structures of Y(NHAr*)$_2$NC (**3**) (left) and Y(NHAr*)$_2$CN (**3'**) (right) using B3LYP/def2-SV(P). All hydrogens are removed for clarity except N–H hydrogens. Light blue, blue, grey, and white spheres represent yttrium, nitrogen, carbon, and hydrogen atoms, respectively.

Table S6. Structural comparisons between crystallographically obtained geometry of Y(NHAr*)$_2$NC **3** and optimised geometry using DFT calculations. Shown here are some characteristic lengths (Å) and angles (°).

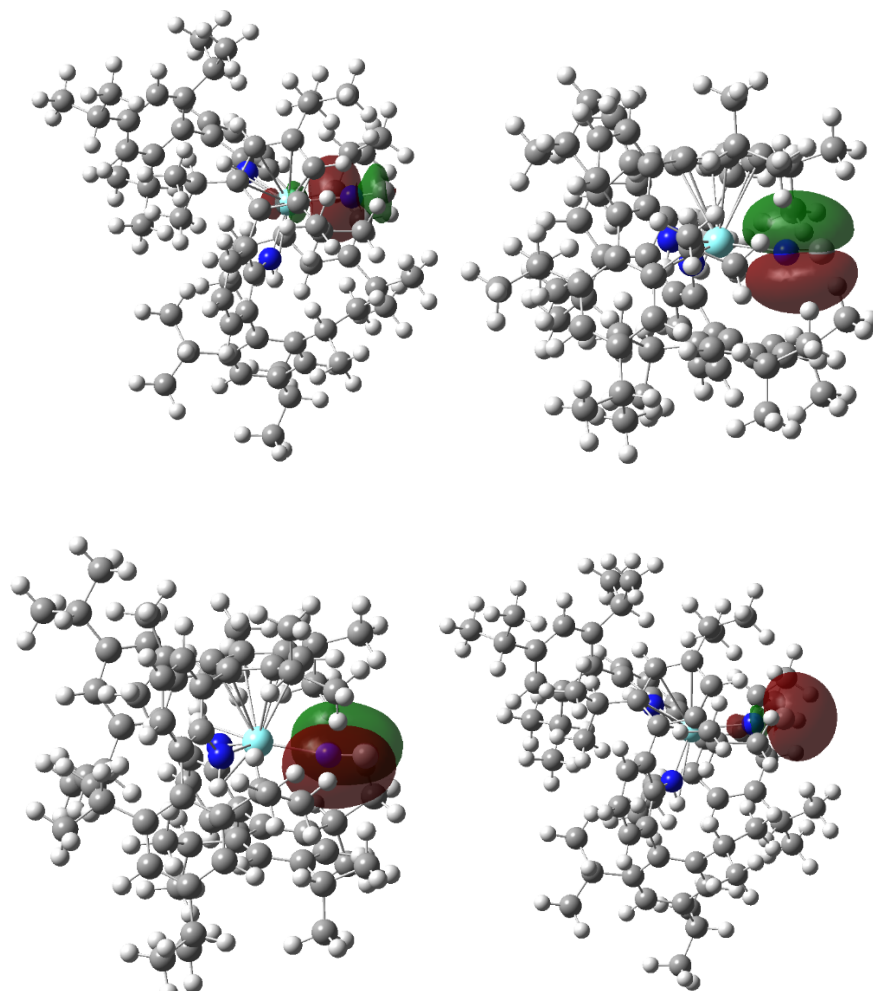| Atoms	Distance (Å)/Angle (°) Experimental	Distance (Å)/Angle (°) Calculated
Y–N2, N3	2.2206(17)	2.2245
	2.2205(17	2.2134
Y-N1	2.3481(18)	2.2785
Y-Ar$_{Cent}$	2.5178(2)	2.603
N1–C1	1.039(4)	1.179
Y–N1–C1		170.33
Y–N–C$_{ipso}$	145.40(15)	139.85
	133.20(14)	134.65
Average C$_{Ar}$–C$_{Ar}$ bond	1.406(3)	1.412

Figure S34. *NBO of N–C bond, N–C (σ-bond; top left), N–C (π-bond; top right), N–C (π-bond; bottom left), and lone pair on C (bottom right) of Y(NHAr*)$_2$NC (**3**). Light blue, dark blue, grey, and white spheres represent yttrium, nitrogen, carbon, and hydrogen atoms, respectively.*

The frequency calculations were carried out to obtain thermochemical data on yttrium isocyanide Y(NHAr*)$_2$NC (**3**) and hypothetical yttrium cyanide Y(NHAr*)$_2$CN (**3'**) structures. The sum of electronic and thermal free energies for Y(NHAr*)$_2$NC (**3**) and Y(NHAr*)$_2$CN (**3'**) are –3041.40663 and –3041.400367 Hartree/particle, respectively. This suggests that the Y(NHAr*)$_2$NC (**3**) structure is thermodynamically more stable (–4 kcal/mol) than the hypothetical Y(NHAr*)$_2$CN (**3'**) structure.

References

(1) W. Clegg, B. Conway, A. R. Kennedy, J. Klett, R. E. Mulvey and L. Russo, *Eur. J. Inorg. Chem.*, 2011, 721–726.

(2) K. Górski, J. Mech-Piskorz, B. Leśniewska, O. Pietraszkiewicz and M. Pietraszkiewicz, *J. Org. Chem.*, 2019, **84**, 11553–11561.

(3) B. Schiemenz and P. P. Power, *Organometallics*, 1996, **15**, 958–964.

(4) J. Gavenonis and T. D. Tilley, *Organometallics*, 2004, **23**, 31–43.

(5) R. K. Harris, E. D. Becker, S. M. C. D. Menezes, R. Goodfellow, and P. Granger, *Pure and Applied Chemistry*, 2001, **73**, 1795–1818.

(6) O. V. Dolomanov, L. J. Bourhis, R. J. Gildea, J. A. K. Howard and H. Puschmann, *J. Appl. Crystallogr.*, 2009, **42**, 339–341.

(7) G. M. Sheldrick, *Acta Crystallogr. Sect. C Struct. Chem.*, 2015, **71**, 3–8.

(8) B. S. Billow, B. N. Livesay, C. C. Mokhtarzadeh, J. McCracken, M. P. Shores, J. M. Boncella and A. L. Odom, *J. Am. Chem. Soc.*, 2018, **140**, 17369–17373.

(9) T. H. Crawford and J. Swanson, *J. Chem. Educ.*, 1971, **48**, 382–386.

(10) G. A. Bain and J. F. Berry, *J. Chem. Educ.*, 2008, **85**, 532–536.

(11) M. Del Mar Conejo, J. S. Parry, E. Carmona, M. Schultz, J. G. Brennann, S. M. Beshouri, R. A. Andersen, R. D. Rogers, S. Coles and M. Hursthouse, *Chem. Eur. J.*, 1999, **5**, 3000–3009.

(12) S. Stoll and A. Schweiger, *J. Magn. Reson.*, 2006, **178**, 42–55.

(13) M. J.Frisch, G. W.Trucks, H. B.Schlegel, G. E.Scuseria, M. A.Robb, J. R.Cheeseman, G.Scalmani, V.Barone, G. A.Petersson, H.Nakatsuji, X.Li, M.Caricato, A. V.Marenich, J.Bloino, B. G.Janesko, R.Gomperts, B.Mennucci, H. P.Hratchian, J. V.Ortiz, A. F.Izmaylov, J. L.Sonnenberg, D.Williams-Young, F.Ding, F.Lipparini, F.Egidi, J.Goings, B.Peng, A.Petrone, T.Henderson, D.Ranasinghe, V. G.Zakrzewski, J.Gao, N.Rega, G.Zheng, W.Liang, M.Hada, M.Ehara, K.Toyota, R.Fukuda, J.Hasegawa, M.Ishida, T.Nakajima, Y.Honda, O.Kitao, H.Nakai, T.Vreven, K.Throssell, J. A.Montgomery, Jr, J. E.Peralta, F.Ogliaro, M. J.Bearpark, J. J.Heyd, E. N.Brothers, K. N.Kudin, V. N.Staroverov, T. A.Keith, R.Kobayashi, J.Normand, K.Raghavachari, A. P.Rendell, J. C.Burant, S. S.Iyengar, J.Tomasi, M.Cossi, J. M.Millam, M.Klene, C.Adamo, R.Cammi, J. W.Ochterski, R. L.Martin, K.Morokuma, O.Farkas, J. B.Foresman and D. J.Fox, Gaussian program suite (revision B01), 2016.

(14) F. Weigend and R. Ahlrichs, *Phys. Chem. Chem. Phys.*, 2005, **7**, 3297–3305.

(15) K. A. Peterson , D. Figgen , M. Dolg and H. Stoll, *J. Chem. Phys.*, 2007, **126** , 124101-124112.

(16) D. G. A. Smith, L. A. Burns, K. Patkowski and C. D. Sherrill, *J. Phys. Chem. Lett.*, 2016, **7**, 2197-2203.

(17) S. Grimme , J. Antony , S. Ehrlich and H. Krieg, *J. Chem. Phys.*, 2010, **132** , 154104.